DIPLOMARBEIT

The 5-HT_{1A} Receptor in Patients with Treatment-Resistant Depression and Healthy Controls

zur Erlangung des akademischen Grades

Diplom-Ingenieur

Im Rahmen des Studiums

Biomedical Engineering

eingereicht von

Christian Milz, BSc.
Matrikelnummer 01618528

ausgeführt am Institut für Analysis und Scientific Computing
der Fakultät für Mathematik und Geoinformatik der Technischen Universität Wien
in Zusammenarbeit mit den Neuroimaging Labs (NIL)
Univ. Klinik für Psychiatrie und Psychotherapie der Medizinischen Universität Wien

Betreuung
AoUniv.-Prof.i.R. PD Dr.sc.med. Dr.techn. Dr.rer.nat. Dipl.-Ing. Frank Rattay
Assoc.-Prof. PD Dr.sc.med. Andreas Hahn, MSc.

Wien, 26.11.2022 _____ _____

Kurzfassung

Positronen-Emissions-Tomographie (PET) spielt eine wichtige Rolle in der Erforschung psychiatrischer Erkrankungen wie etwa Depression. Während mehrere Studien den Zusammenhang zwischen dem inhibitorischen Serotonin Rezeptor 5-HT_{1A} und Depression belegen, ist dessen Verhalten bei behandlungsresistenter Depression noch wenig erforscht. Das Ziel dieser Arbeit ist es die Bindung am 5-HT_{1A} Rezeptor zwischen einer Gruppe von Personen mit behandlungsresistenter Depression (n = 20) und einer gesunden Kontrollgruppe (n = 20) zu vergleichen. Dazu wurden T1 gewichtete Magnetresonanztomographie Scans und PET-Scans mit dem Tracer [*carbonyl-*^{11}C]WAY-100635 aus insgesamt drei Studien entnommen. Die Bilddaten wurden in MATLAB unter der Verwendung der Statistical Parametric Mapping 12 (SPM12) Software verarbeitet, um einen Vergleich zwischen den Gruppen zu ermöglichen. Das Bindungspotential (BP_{ND}) wurde mittels eines multilinearen Referenz Gewebe Modells bestimmt. Dabei wurde die weiße Substanz des Kleinhirns als Referenz-Region verwendet. Die weitere statistische Auswertung wurde für fünf Gehirnregionen mit bekannt hoher Rezeptordichte (Insula, Hippocampus, Orbitofrontalkortex, Amygdala und vorderer Teil des Gyrus cinguli) durchgeführt. Eine Varianzanalyse (ANOVA) mit Messwiederholung zeigte einen signifikanten Effekt von Gruppe und Gehirnregion auf BP_{ND} aber nicht von deren Interaktion. Des weiteren unterstützen post-hoc Tests die Hypothese, dass Patient:innen mit behandlungsresistenter Depression signifikant niedrigeres BP_{ND} als die Kontrollgruppe aufweisen. In der Literatur finden sich ähnliche Ergebnisse für Studien an Personen mit Depression. Die Ergebnisse zeigen somit die Relevanz des 5-HT_{1A} Rezeptors für behandlungsresistente Depression.

Abstract

Positron emission tomography (PET) investigations of the serotonergic system have yielded important insights into psychiatric disorders such as major depressive disorder (MDD). Treatment resistant depression (TRD) describes a subtype of MDD, characterised by lack of response to treatments of two classes of antidepressants. While the main inhibitory serotonin receptor (5-HT_{1A}) has been shown to be involved in the pathology of MDD, alterations in TRD are still not completely understood. The aim of this thesis is to compare 5-HT_{1A} receptor binding in TRD patients (n = 20) to healthy controls (HC) (n = 20). In this cross-sectional analysis, PET scans with the radiotracer [*carbonyl-*^{11}C]WAY-100635 and T1 weighted magnetic resonance imaging data were selected from a total of three studies. Groups were matched by age and sex. Realignment, co-registration of PET to MRI and normalisation to a standardised MNI space were performed in MATLAB using the Statistical Parametric Mapping 12 (SPM12) software. The nondisplaceable binding potential (BP_{ND}) was then modelled with the multilinear reference tissue model 2, using cerebellar white matter as reference region. Statistical analysis was performed on BP_{ND} in five regions of interest (insula, hippocampus, orbitofrontal cortex, amygdala and anterior cingulate cortex) that have been found to exhibit high density of binding sites. A repeated measures analysis of variance (ANOVA) found a significant effect of group and region on BP_{ND} but not for their interaction. Post-hoc tests support the hypothesis that BP_{ND} is lower in TRD patients. Other studies on the distribution of the 5-HT_{1A} receptor in MDD populations found similar results. Thus, these findings provide further evidence of the 5-HT_{1A} receptor's relevance for TRD.

Acknowledgements

First, I would like to thank Frank Rattay and Andreas Hahn for supervising this thesis. Also, I want to express my gratitude towards Matej Murgaš for taking the time to guide me through the entire process. Moreover, I thank the Neuroimaging Labs (head: Prof. PD Dr. Rupert Lanzenberger) for the opportunity to carry out the master's thesis and for kindly providing the dataset.

Table of Contents

1 Introduction

Psychiatric disorders, especially depressive and anxiety disorders, have got more into the focus of the public due to the significant increase in patient numbers since the beginning of the SARS-COV-2 pandemic in early 2020 (Shah et al., 2021; WHO, 2022b). Among these disorders, depression shows high mortality, an increasing prevalence and is often referred to as one of the leading causes of disabilities (Kaufman et al., 2016).

Generally, events that affect everyday life in a drastic way and introduce a great deal of uncertainty such as pandemics, but also more recently the war in the Ukraine, are linked to an increase in anxiety and depressive disorders (Dar et al., 2017). However, it is important to bear in mind that these disorders exist in a substantial part of the population, whether or not the wide public is made aware of the issue by extraordinary events. This is especially relevant to highlight because even in the years before the pandemic, a rising trend in case numbers had been reported for at least the last decade. This was shown globally and also specifically in Austria (Global Burden of Disease Collaborative Network, 2020). The prevalence of depression in the Austrian population in relation to other chronic diseases can be seen in **Figure 1**. According to a report from 2019 commissioned by the Austrian federal ministry for social affairs, health, care and consumer protection, 5.7% of men and 9.2% of women reported that they suffered from depression at one point in the last 12 months (Klimont, 2020). This translates to approximately 660,000 afflicted in Austria and over 300 million worldwide.

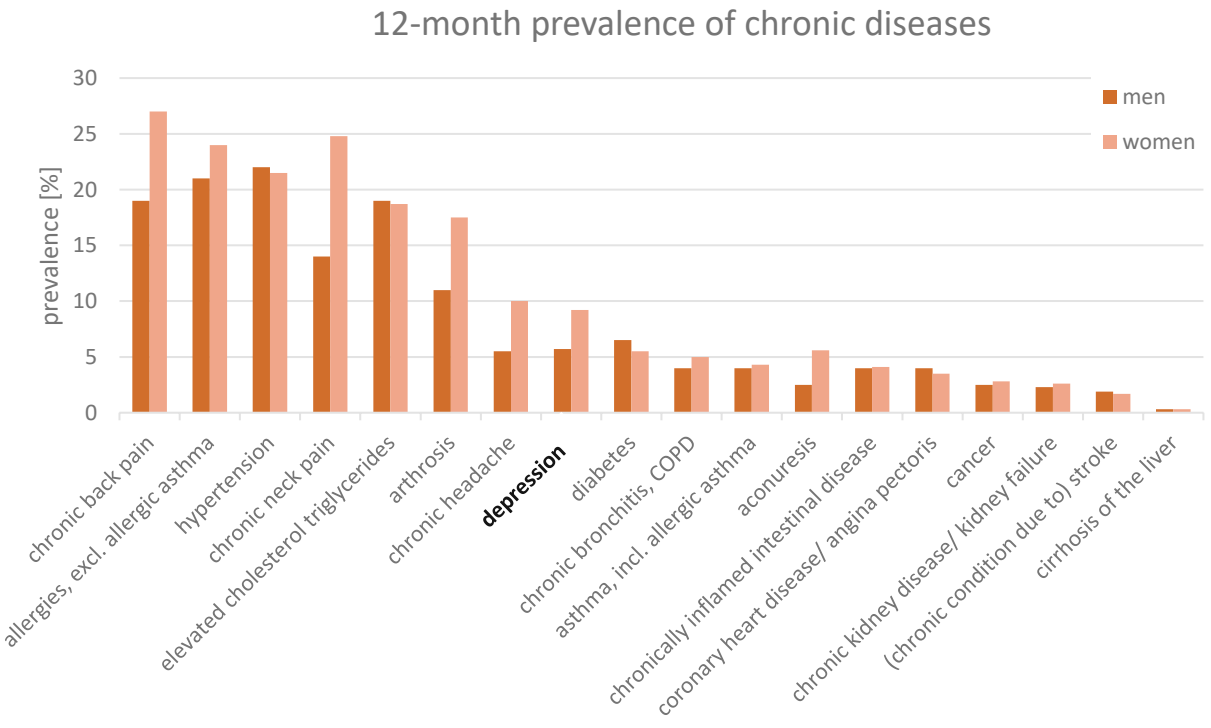

Figure 1: *twelve-month prevalence of selected chronic diseases in 2019 in Austria; based on* (Klimont, 2020)

Among other sources, the World Health Organisation's (WHO) International Classification of Diseases (ICD) and the American Psychiatric Association's Diagnostic and Statistical Manual of Mental Disorders (DSM), provide criteria for diagnosis of disorders and diseases. Despite these extensive works, it has been recognised that especially in the case of mental disorders, such as depressive and anxiety disorders, symptoms may not fall into just one category (American Psychiatric Association, 2022).

Colloquial use of the word depression may be misleading, as in this context it often refers to momentary feelings of sadness or listlessness. However, in medical literature, depression does not refer to a disease itself but rather a syndrome. The very broad field of associated disorders include major depressive disorder (MDD), substance-induced depressive disorder or disruptive mood dysregulation disorder (American Psychiatric Association, 2022). Experienced symptoms include but are not limited to being sad, irritable, feelings of emptiness and limited capacity to function (American Psychiatric Association, 2022; WHO, 2022a). By highlighting the reduced capability to function, it becomes clear why depressive disorders are considered disabilities. In 2007 the United Nations in the Convention on the Rights of Persons with Disabilities (UN General Assembly, 2007, p. 4) gave the following definition for disability:

> "Persons with disabilities include those who have long-term physical, mental, intellectual or sensory impairments which in interaction with various barriers may hinder their full and effective participation in society on an equal basis with others."

More precise diagnostic criteria are provided for each specific instance of depressive disorder. The severity of these disorders must not be underestimated, because not only are they the source of severe personal suffering but can also be considered as fatal in many cases. Depression has generally been found to represent a risk factor for suicide ideation (Ribeiro et al., 2018) and is associated with increased suicidal behaviour through its link to psychological pain (Conejero et al., 2018). Thus, it is important to gain a better understanding of the associated pathological alterations in the human brain.

As mentioned above, awareness for mental illness is increasing overall, which can be partly accredited to a rise in prevalence. However, the more specific condition of treatment resistant depression (also treatment refractory depression) (TRD) is less known. The term TRD in literature is mainly associated with MDD. In addition to the general symptoms as described previously for depressive disorders, these further criteria have to be met for a positive diagnosis of MDD. Over the duration of two weeks, at least five of a list of nine symptoms (such as depressed mood, significantly reduced interest, weight loss, insomnia, hypersomnia, etc.) must be present. Moreover, these symptoms have to represent a change from previous functioning (American Psychiatric Association, 2022).

Antidepressants are the first line of treatment and psychotherapy is an essential additional option for patients suffering from MDD (Pandarakalam, 2018). A single line of treatment may require several forms of adjustments such as modification of dosage but will ideally lead to a full symptom remission with minimal side effects. Still, in 20 to 40%

of patients no satisfactory treatment response is achieved (Shelton et al., 2007). Nevertheless, MDD is not considered to be treatment resistant after only one treatment trial. A uniform definition of TRD remains to be found (Bartova et al., 2019; Dold & Kasper, 2017). However, attempts to give a definition either use failure to decrease the Hamilton depression total score below a threshold or that a patient is still failing to show remission after two adequate antidepressant trials (Dold & Kasper, 2017; Fornaro & Giosuè, 2010). Preclinical studies suggest that TRD patients may benefit from a shift in treatment procedure from antidepressant trials to electroconvulsive therapy (Lanzenberger et al., 2013).

Tools such as self-reporting of symptoms and certain scales derived from that (e.g. HAMD total score) are well established in the context psychological disorders. Nevertheless, given the time it takes for one treatment (or, in case of non-responding patients, several treatment options) to take effect, the benefit of finding additional indicators of treatment resistance early on, is obvious. Although imaging is not yet as well established in psychiatry as it is in other disciplines such as oncology (Lui et al., 2016), it may provide invaluable complementary insights.

In the field of neuroimaging, a wide variety of technologies such as magnetic resonance imaging (MRI), Positron emission tomography (PET) and single photon emission computed tomography (SPECT) are available. Just like the physical principles of the imaging modalities vary greatly, also the information derived from them shows a large bandwidth. For magnetic resonance imaging, T1 weighted images provide high-resolution structural information of grey matter whereas diffusion tensor imaging and magnetisation transfer imaging are used to image cerebral white matter (Lui et al., 2016). These images do not only provide information on the current brain anatomy, but they are also used to track changes over time, which is a similarly important information. Discerning pathological changes to the brain is made more complicated by the circumstance that also the healthy brain shows significant changes over the course of childhood and adolescence as well (Lui et al., 2016; Vanes & Dolan, 2021).

Besides structural information, functional imaging provides a significant addition. Commonly applied modalities are fMRI and PET. fMRI can be applied to investigate brain activation during task and resting state or may be used for studies of brain connectivity (Vanes & Dolan, 2021). In contrast to fMRI, PET is used to investigate brain metabolism and chemistry (Lui et al., 2016). A small selection of applications for PET includes studies of glucose metabolism, dopamine synthesis and investigations of the serotonergic system (Mitelman, 2019; Turkheimer et al., 2014). A more detailed look at the working principles of PET and MRI are presented in **Sections 2.1** and **2.2** respectively.

Research in the field of depression has been linked to the serotonergic system, and especially the main inhibitory serotonin receptor 5-hydroxytryptamine-1A (5-HT_{1A}) has been a subject of interest (Albert & Lemonde, 2004; Farde et al., 1998; Savli et al., 2011). Generally, serotonin plays an important role in the central nervous system as a modulatory neurotransmitter, marking it as a substance of interest for psychiatric research (Saulin et al., 2012). For the 5-HT_{1A} receptor, studies with the radiotracer [*carbonyl*-^{11}C]WAY-100635 have shown high affinity and selectivity (Farde et al., 1998). WAY-100635 has been found to be a 5-HT_{1A} antagonist (Farde et al., 1998) displaying

reversible binding characteristics (Forster et al., 1995). Several studies have shown high tracer binding in the insula (INS), hypothalamus (HIP), amygdala (AMY), anterior cingulate cortex (ACC) and orbitofrontal cortex (OFC) (Albert & Lemonde, 2004; Farde et al., 1998; Lanzenberger et al., 2013; Savli et al., 2012).

In sum, the 5-HT1A receptor has high implications in the pathophysiology of MDD. However, there is little data available of this receptor in TRD. Therefore, this work aims to further our understanding of alterations to the distribution of 5-HT_{1A} receptors in TRD patients. For this aim, we compare brain-imaging data obtained with PET of a healthy control and a TRD subject population. Based on previous research on the distribution of the 5-HT_{1A} receptor (Albert & Lemonde, 2004; Farde et al., 1998; Lanzenberger et al., 2013; Savli et al., 2012) we hypothesise a significant decrease in binding of [*carbonyl*-^{11}C]WAY-100635 in INS, HIP, AMY, OFC and ACC in the TRD group compared to the healthy controls.

2 Technical Background

2.1 Magnetic Resonance Imaging

Magnetic resonance imaging provides high resolution structural images but can also be used for functional imaging. It is a non-invasive method of analysing soft tissue and unlike many other imaging modalities such as computed tomography, SPECT or PET that are applied in medical imaging, MRI does not use ionising radiation (Song, 2014; Yousaf et al., 2018).

2.1.1 Physical Principle

MRI is based on the phenomenon of nuclear magnetic resonance (NMR), that was first described in 1938 by Rabi I. Isidor and further refined by Felix Bloch and Edward M. Purcell (Rinck, 2008; Song, 2014). At its core, NMR explains how atomic nuclei absorb radiofrequency (RF) energy in a magnetic field and reemit it at a characteristic/resonant frequency. In the case of clinical MRI, the nuclei of hydrogen atoms are of interest due to their natural abundance in the human body in fat and water (Song, 2014).

Without a magnetic field present, the magnetic moments (spins) are randomly orientated and there is zero net magnetisation (M). When an external magnetic field ($\mathbf{B_0}$) (in this and following sections, vectors are written in bold letters) is applied, spins align (anti-) parallel to it. Moreover, the spins will begin to preces about the orientation of $\mathbf{B_0}$ at a frequency referred to as the Larmor Frequency (ω_0). The rotation of spins is illustrated in **Figure 2**. The Larmor Frequency, which is the precession frequency, is linear proportional to the applied magnetic field. For a hydrogen nucleus in a magnetic field of 3 T (commonly found in clinical scanners), **Eq. (1)** (where γ is the gyromagnetic constant) yields a resonant frequency of 127.44 MHz. As mentioned above, the frequency lies within the RF range (Kuperman, 2000; Song, 2014).

$$\omega_0 = \gamma B_0 \qquad (1)$$

While the spins rotate about the stationary magnetic field, the net magnetization is stationary and orientated along the constant $\mathbf{B_0}$. Only when an additional alternating magnetic field ($\mathbf{B_1}$) is applied, does it start to nutate about the net magnetic field's axis. $\mathbf{B_1}$

is typically only applied for a short time (see **Section 2.1.2**). A RF coil provides a simple means to measure the resulting signal via the current that is induced according to Faraday's law (Song, 2014). Ultimately, that means, that MRI measures the tissue magnetisation. Tissue with high magnetisation will display as hyperintense (bright) whereas areas with little to no magnetisation will appear hypointense (dark) (Sprawls, 2000).

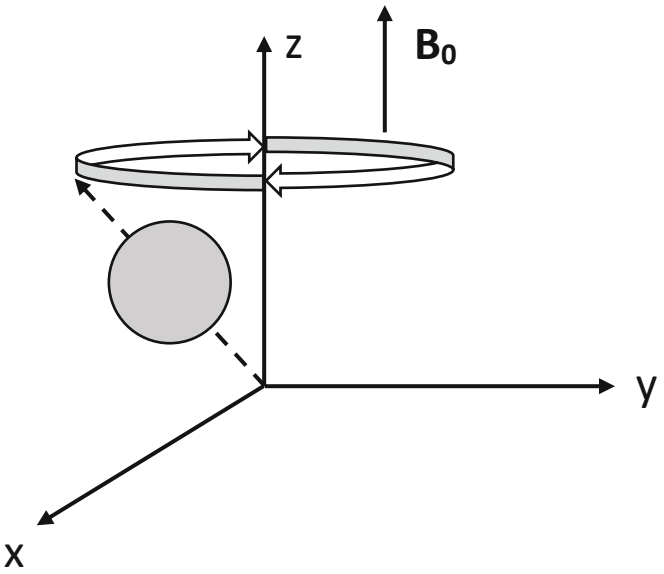

*Figure 2: The atomic nucleus' spin precesses around the direction of the magnetic field (**B_0** along the z-axis) at the Larmor frequency. adapted from* (Song, 2014)

After the $\mathbf{B_1}$ is deactivated, the longitudinal component of the magnetisation ($\mathbf{M_z}$) begins to relax towards its original position of minimum energy along $\mathbf{B_0}$. The return to this initial state follows an exponential decay and is characterised via the time constant T1. This is referred to as spin-lattice relaxation. T1 is influenced by the surrounding material and hence holds information about the type of tissue (Yousaf et al., 2018). In other words, the tissue-specific spin-lattice relaxation is one means to provide contrast in magnetic resonance imaging (Sprawls, 2000).

The precession about the net magnetic field and thus the transversal magnetisation ($\mathbf{M_{xy}}$) component is affected as well by the deactivation of the alternating field. The individual spins can be seen as dipoles that interact with each other and perturb the precession of other spins in their vicinity. That is why the process is referred to as spin-spin relaxation. This causes continuous changes to the precession frequency of the individual spins. The resulting loss of phase coherence and hence signal follows an exponential decay with a time constant T2. Since T2 is another tissue property, it provides an additional type of contrast similar to T1 (Song, 2014).

Yet another type of contrast in MRI is provided via the proton density (PD). As established above, in MRI the magnetisation of hydrogen nuclei generates the measured signal. Therefore, tissues with higher PD correspond to more magnetisation and will display brighter in the final image (Sprawls, 2000).

Eq. (2) and **(3)** show the exponential behaviour of spin-lattice and spin-spin relaxation over time. The equations clearly show that the T1 weighted signal increases towards its original value before RF excitation ($\mathbf{M_z}(0)$) whereas the transverse magnetisation ($\mathbf{M_{xy}}$) decays towards zero. In **Figure 3**, signals of different tissues are shown to better visualise the signal characteristics of the two processes. It is apparent that spin-spin relaxation is faster than spin-lattice recovery. For example, white matter shows a T1 of 790 ms whereas its T2 has only a value of 90 ms (Song, 2014). We also see that fat recovers faster to its original state of $\mathbf{M_z}$ while cerebrospinal fluid (CSF) has the longest T1 of the shown brain tissues. In addition to the temporal behaviour of the two signals, **Figure 3** shows also how the tissue will be displayed in the rightmost column (signal intensity). From that we see that in the brain, fat reconstructs the brightest and decreasing intensity for white matter, grey matter and finally CSF is found. Additionally, it can be observed that T1 values increase for increasing field strength, whereas no such effect on T2 can be observed (Bushberg et al., 2012).

$$\boldsymbol{M_z}(t) = \boldsymbol{M_z}(0)e^{-t/T_1} + \boldsymbol{M_0}(1 - e^{-t/T_1}) \qquad (2)$$

$$\boldsymbol{M_{xy}}(t) = \boldsymbol{M_{xy}}(0)e^{-t/T_2} \qquad (3)$$

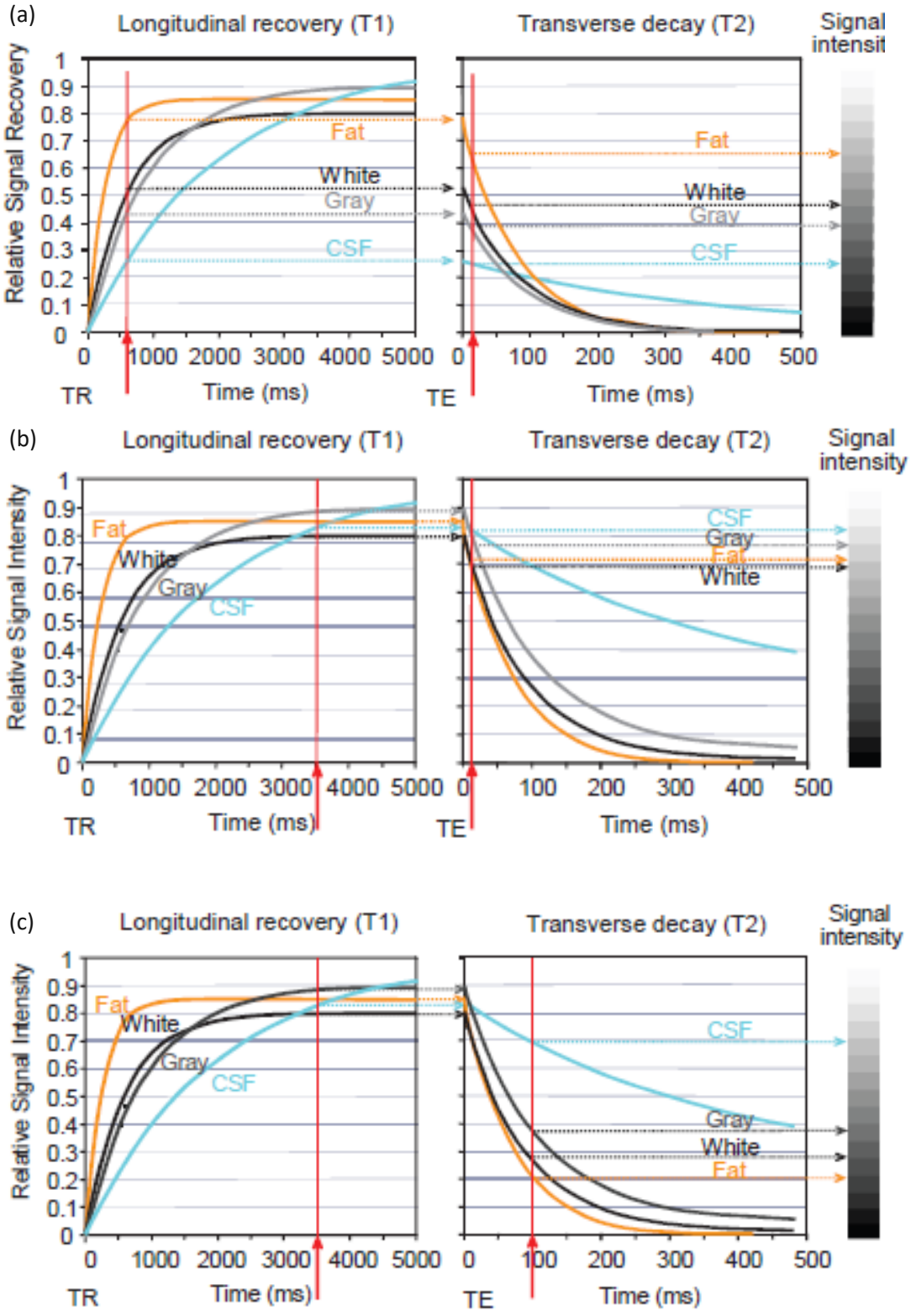

Figure 3: *longitudinal recovery and transverse decay shown for fat, white matter, grey matter and cerebrospinal fluid (CSF); time given in ms after TR or TE; vertical red lines indicate the choice of TR and TE for T_1 weighting* ***(a)****, PD weighting* ***(b)*** *and T2 weighting* ***(c)****; taken from* (Bushberg et al., 2012)

2.1.2 Tissue Contrast and Spatial Encoding

The dominant type of contrast depends on the imaging protocol and the acquired image is labelled accordingly (e.g. T1 weighted image) (Sprawls, 2000). The imaging process can be divided into two major phases (see also **Figure 4**). One is linked to the longitudinal magnetisation (T1 contrast) and the other to transverse magnetisation (T2 contrast). PD contrast is generally present but may be dominated by T1 or T2 contrast (Sprawls, 2000). Several acquisition parameters define the weighting of the image. The time of repetition (TR) states the time between B_1 excitation pulses. It is also the time between acquisition of individual slices in a volume and encompasses the T1 recovery and T2 decay (Bushberg et al., 2012).

As previously mentioned, spins start to acquire a phase lag with regard to each other, following excitation. To counteract the accompanying loss of M_{xy} signal, a 180° refocusing pulse can be applied. As a consequence, spins with the largest phase advance will now have the largest lag and vice versa. At some time after the flipping of the spins, M_{xy} reaches a maximum when all spins align before they start to de-phase again. The maximum is referred to as the spin echo and the time between RF pulse and echo is referred to as time of echo (TE) (Bushberg et al., 2012; McRobbie et al., 2006).

Several pulse sequences are available for magnetic resonance imaging such as spin echo (SE), inversion recovery and gradient echo. Here, only a closer look at SE will be provided. The key features are an initial 90° RF pulse and a subsequent 180° RF pulse at TE/2 that generates the spin echo. The effect of the 180° pulse is a reversal of the phase accumulation caused by inhomogeneity of the field. It is also referred to as a refocusing, that occurs at TE when the accumulated phase cancels out (Song, 2014). A schematic overview of a SE sequence is shown below in Figure 5. In addition to the relative timing of 90°, 180° pulse and spin echo, the lower part of the figure displays additional information. The gradients (G_z, G_y and G_x) are discussed later in this chapter.

Figure 3 indicates proper choice of TE and TR (red vertical line) for T1 weighted imaging. This can intuitively be derived by looking at the signal characteristics of the different tissues. Depending on which contrast should be most prominent, TE and TR are chosen accordingly. For T1 contrast largest difference is found shortly after the RF pulse (i.e. for a short TR). The same applies for the transverse decay, meaning TE should be chosen to be relatively short as well. As a result, the largest amount of tissue contrast will be due to different T1. Evidently, the same line of reasoning applies to T2 and PD contrast (see also **Figure 3b-c**). This rationale is also well illustrated in **Figure 4**, where times of highest contrast due to T1, T2 and PD are shown.

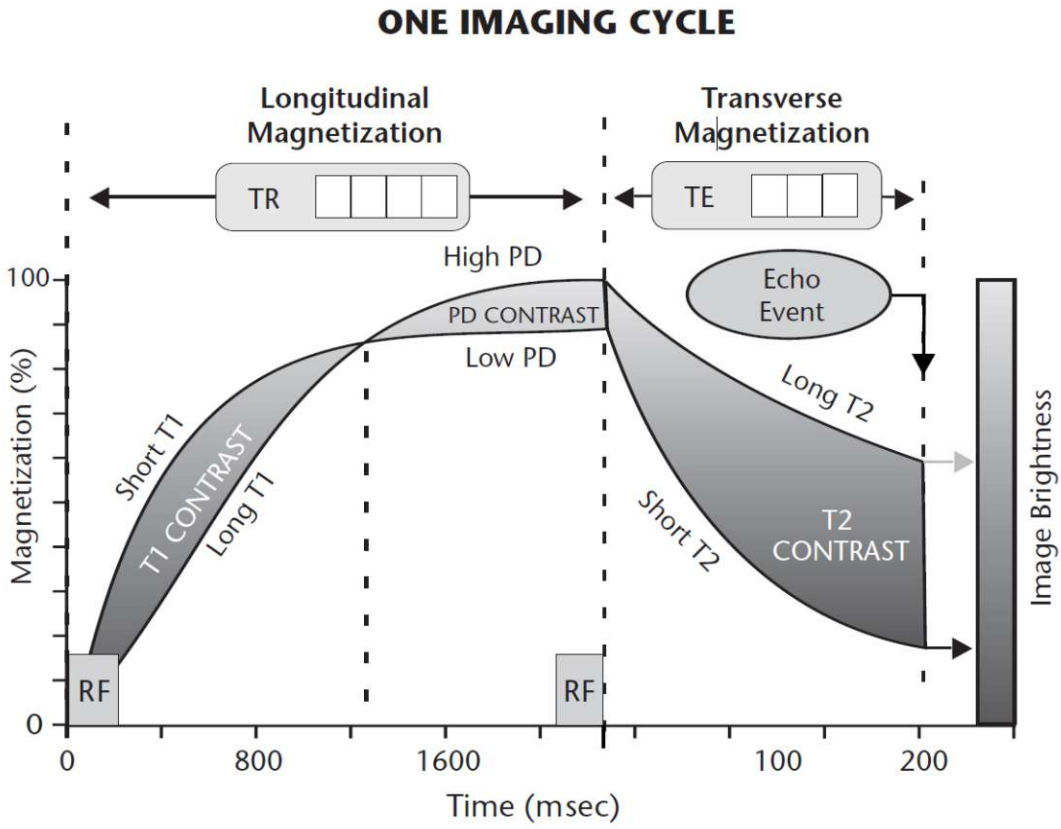

Figure 4: *full MR imaging cycle; Acquisition parameters (TR, TE) as well dominant type of are indicated. taken from* (Sprawls, 2000)

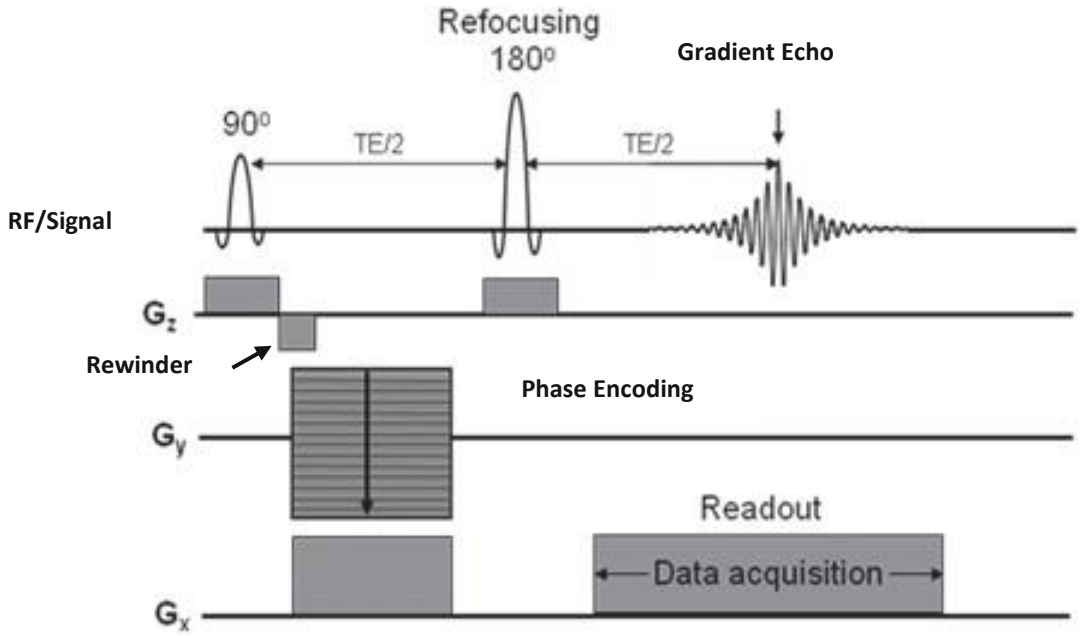

Figure 5: *SE sequence; 180° RF pulse for refocusing at TE/2; taken from* (Song, 2014)

Even with the different options for selecting tissue contrast that were discussed, a major aspect has been omitted so far, namely the localisation of the signal. In order to reconstruct a meaningful image, signals need to be assigned to individual voxels. This can be achieved by applying magnetic field gradients in addition to the B_0 field (Bushberg et al., 2012; Song, 2014).

Once more referring to the equation of the Larmor frequency (**Eq. (1)**), it shows the implications of such a gradient field ($\nabla\mathbf{B}$). The superposition increases or decreases the net magnetic field at any given location and with it, the spins' precession frequency (Bushberg et al., 2012). Looking at only one gradient (e.g. z-direction), we see that an applied RF pulse can only excite one single plane/slice along the direction of the gradient. This slice will be along a plane perpendicular to the net gradient (Sprawls, 2000). After slice selection has been performed in this way, the first gradient is deactivated.

As a next step, localisation within the selected slice is performed. A short gradient perpendicular to the first one, temporally assigns different precession frequencies along its direction. Upon deactivation of the gradient this results in increasing phase along the gradient. In regions of higher frequency during the applied gradient, more phase will have gathered compared to regions that displayed a lower frequency (Song, 2014). Lastly, a final frequency-encoding gradient along the remaining coordinate axis is applied. This is performed during the echo event (emission of the signal). With these three encodings (slice, phase, frequency) each voxel can be uniquely identified (Bushberg et al., 2012; Sprawls, 2000).

A concise diagram of the encoding discussed in the last paragraphs is shown in **Figure 5** alongside with the SE sequence. The 90° RF pulse is used for slice selection and is followed by a phase rewinder. Similar to the process during phase encoding, the first gradient (G_z) also leads to an accumulation of phase but is unwanted at the stage of slice selection. A gradient (phase rewinder) of opposite polarity is applied in order to reverse this process. Another gradient thus far not discussed is the pre-phase gradient. Without going into further detail, it is applied before readout and results in the k-space being filled symmetrically (Song, 2014).

The shown process needs to be repeated for the number of desired slices. The only difference is that for each subsequent slice, the RF-pulse needs to be adjusted to correspond to a different resonant frequency. Slice order can be adjacent slides from beginning of either side of the volume or interleafed (Song, 2014).

2.1.3 MRI Hardware

The main aspects for MRI such as the magnetic field (B_0), gradient fields and RF excitation have been discussed in the previous sections. This chapter gives an overview of the associated hardware.

Figure 6 lists the main components of a clinical MRI scanner. The patient generally is placed horizontally on the bed lying supine. The patient bed is aligned along the axis of $\mathbf{B_0}$. In clinical scanners generally superconducting magnets are used for creating the main magnetic field. By cooling the coils of an electromagnet with liquid helium to approximately 4K (-269°C), the conducting material's electrical resistance drops to zero, allowing the current to be ramped up to achieve the desired magnetic field strength (Bushberg et al., 2012). Only due to superconductivity, high enough currents can be generated to achieve the required magnetic flux density in the range of several Tesla. The low temperature needs to be maintained at all times in order to prevent rapid boiling and evaporation of liquid helium due to resistive heating (Kuperman, 2000). The superconducting coil and the cooling system (cryo-compressor, cryostat with liquid and gaseous helium) are also shown in **Figure 6**.

Although, the main coil is designed in a way to provide a maximally homogenous magnetic flux over the whole volume, additional shim coils are used to provide homogeneity of about 1 ppm. Besides the magnet design, the patient introduces inhomogeneity as well (Leach, 2014). The shim coils are placed within the bore of the main magnet and superimpose their auxiliary magnetic field over $\mathbf{B_0}$ to cancel spatial variations (Kuperman, 2000).

The in **Section 2.1.2** extensively discussed magnetic field gradients are produced by gradient coils that are placed within the bore of the main magnet. The in comparison to $\mathbf{B_0}$ (e.g. 3 T) relatively small gradients (in the range of mT/m) are achieved by supplying a direct current to a set of two or more gradient coils (Kuperman, 2000). A commonly used coil-geometry are Golay coils for the x and y gradients (orthogonal to $\mathbf{B_0}$) and a pair of coils placed coaxially with the main magnet's windings for the z-gradient. The gradient coils need to be supplied with strong currents in the range of hundreds of Amperes (Leach, 2014).

While the superconducting magnet supplies the strong $\mathbf{B_0}$ and the gradient coils are used for spatial encoding, radiofrequency coils are used to excite magnetisation and detect signal from the patient. They are placed within the main magnet's bore alongside the gradient coils (see **Figure 6**). The same set of coils can be used as transmitter and receiver or dedicated coils may be used for each function (Kuperman, 2000). The RF coils generate the radiofrequency pulse to modulate the Larmor frequency. The signal, that is emitted by the patient is significantly smaller than the excitation pulse (can be in the range of 15 kW), which necessitates the protection of the receive channels from the transmitted power and several amplification steps (Leach, 2014).

Other MRI scanner components that are listed in **Figure 6** are the sequence controller and connection to the picture archiving and communication system (PACS).

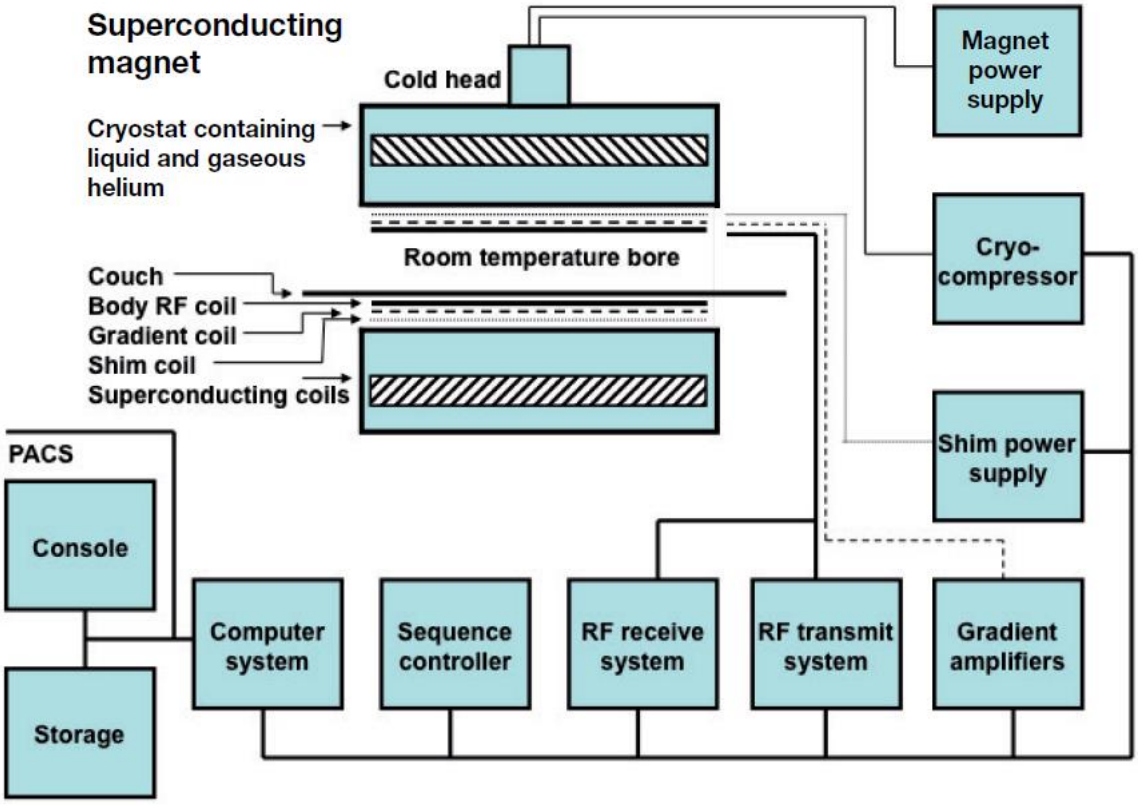

***Figure 6**: hardware components of a clinical MRI scanner; taken from* (Leach, 2014)

2.1.4 Artefacts

Artefacts cause changes to signal intensities and do not represent any true structure or function of the body (Sprawls, 2000). Therefore, they degrade the data quality and reducing artefacts is an important step to achieve high image quality. If not corrected properly, the diagnostic potential is inhibited by the obscuring or mimicking of structures. Common sources of artefacts are errors in the spatial encoding, patient movement, inhomogeneity of the magnetic field or metal objects (Bushberg et al., 2012; Kuperman, 2000; Leach, 2014; Sprawls, 2000).

The chemical shift effect describes how the Larmor frequency of hydrogen nuclei in water and fat differ. The discrepancy is caused by shielding of the magnetic field due to molecular structure and electron orbital characteristics and results in a difference in

resonant frequency of about 3.5 parts per million (Bushberg et al., 2012; Kuperman, 2000). As a consequence of the differing resonant frequencies of water and fat, these structures can be shifted apart, if localisation is based on frequency. The frequency separation increases for larger field strengths. One way to mitigate the effect of the chemical shift artefact is to use a bandwidth per pixel similar to the frequency separation between the two tissues (Leach, 2014). **Figure 7** shows an overview of the issue of chemical shift. As the magnetic field strength is increased, also the spectral shift in resonance frequency between water and fat increases.

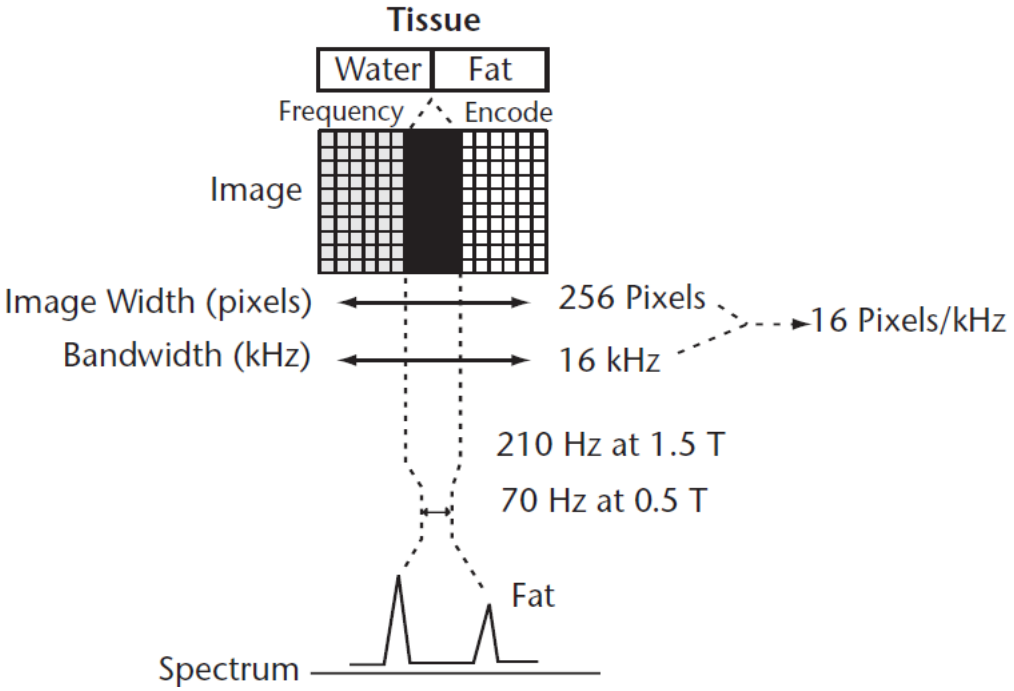

***Figure 7**: visualisation of the chemical shift artefact; Water and fat display different resonant frequencies and consequently are shifted along the phase encoding direction. taken from* (Sprawls, 2000)

Movement related artefacts are easily explained. The imaged subject moves during acquisition, either due to involuntary physiological processes such as breathing or voluntary movement like adjusting the body position. The results are alterations to amplitude and phase which can manifest as considerable image blurring and ghost images (**Figure 8 (a)**) (Bushberg et al., 2012; Kuperman, 2000). Motion artefacts are mainly present along the direction of phase encoding. Movement artefacts due to repeated physiologic movement can be reduced by gated acquisition (Leach, 2014). This means that image acquisition is performed during the same time of e.g. the breathing cycle. Also signal averaging and short TE spin echo sequences are suitable methods (Bushberg et al., 2012). Generally, movements may also be corrected during processing after acquisition. Realignment is such a processing step (see **Section 3.3** for more information).

Aliasing is another relevant artefact. It is caused by structures that lie outside the field of view (FOV), but have the same frequency and phase characteristics as parts within the FOV (Sprawls, 2000). As a result, areas just outside the field of view appear wrapped around to the other side of the image. **Figure 8 (b)** shows how the nose, that lies outside the FOV to the right, is incorrectly displayed on the left side of the image. This happens due to under-sampling or nonlinear gradients. The issue of under-sampling is the same as for other modalities when the Nyquist sampling limit is exceeded, i.e. frequencies of the signal that exceed half of the sampling frequency are present. As is often the case when dealing with this issue, a lowpass filter alleviates the problem by limiting the frequencies in the acquired signal to a range where the Nyquist theorem is not violated. Increasing the number of phase encoding steps has a similar effect. Proper placement of the region of interest in the FOV is also an important aspect in reducing the wrap-around effect (Bushberg et al., 2012).

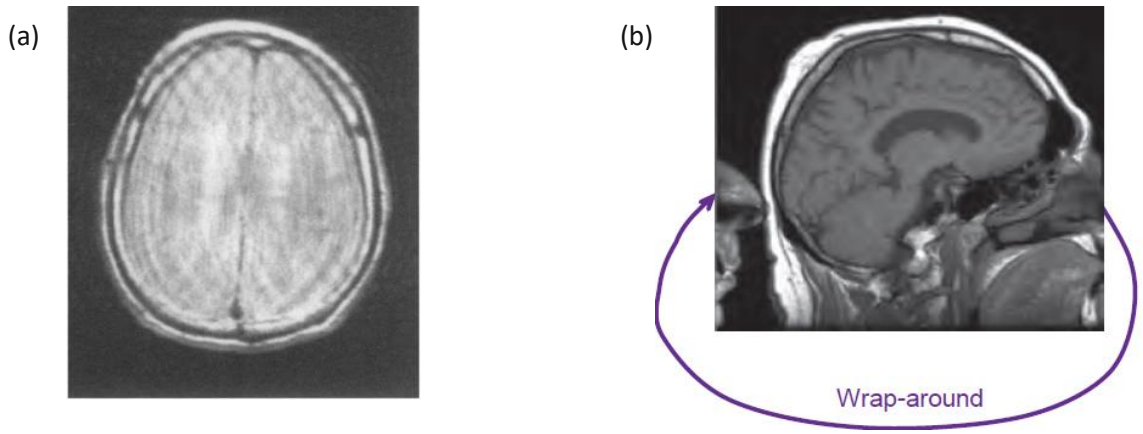

Figure 8*: examples of two commonly found artefacts in MRI:* ***(a)*** *strong blurring and ghost images of spin-echo image of the head due to patient movement during acquisition; taken from* (Kuperman, 2000) ***(b)*** *wrap-around or aliasing artefact: The nose outside the FOV is displayed on the opposite side of the image; taken from* (Bushberg et al., 2012)

2.2 Positron Emission Tomography

Positron emission tomography is a quantitative imaging modality that is applied in nuclear medicine. At its core, PET uses radioactive decay in order to acquire images of biological processes in the body. This sets nuclear imaging apart from modalities such as MRI, which provide structural information (Cherry et al., 2012).

2.2.1 Physical principle

In PET, the gamma radiation that is used for construction of the image comes from the annihilation of an electron with its antiparticle, the positron. β^+ emitters are used. A generalised formulation of a positron decay is shown in **Eq. (5)**. The unstable radionuclide converts a proton to a neutron (**Eq. (4)** and becomes stable due to the decrease in atomic number (Z). The conversion of a proton (p^+) to a neutron (n) also results in the production of a positron (e^+) as well as a neutrino (ν) and energy (Q) is released. **Eq. (5)** indicates the missing proton as a decrease in atomic number by one, the rest of the equation is the same as in **Eq. (4)**.

$$p^+ \rightarrow n + e^+ + v + Q \qquad (4)$$

$${}^{A}_{Z}X \rightarrow {}_{Z-1}{}^{A}Y + e^+ + e^- + v \qquad (5)$$

Charge is typically conserved by emission of an orbital electron via internal conversion (Maisey, 2005). Recombination of an electron with its antiparticle results in an annihilation, during which the two particles are converted to energy. A positron typically travels a few millimetres from its place of origin, until it annihilates. The mean path travelled before annihilation depends on the nuclide and medium (Turkheimer et al., 2014). An overview of radionuclides typically used in PET alongside their respective travelled distance in water can be found in **Table 1.** For the listed radionuclides, mean range in water before annihilation occurs is in the range of 0.6 to 2.5 mm.

The energy freed during annihilation is released as two photons of approximately 511 keV each (see also Eq. **(6)**), travelling in opposite direction at almost exactly 180°. The latter property is exploited in localising the decaying nucleus. Deviations from the expected energy of 511 keV, which corresponds to the rest-mass equivalent of the particles, can be accredited to non-zero kinetic energy before annihilation.

Similarly, non-zero momentum before annihilation introduces uncertainty in the angle between the two photons (Maisey, 2005).

$$e^- + e^+ \rightarrow \gamma(2x\ 511\ keV) \quad (6)$$

Table 1: selected radionuclides listed with their half-lives ($t_{1/2}$), maximum and mean range in water until annihilation; adapted from (Maisey, 2005)

nuclide	$t_{1/2}$ (minutes)	range in water (mm)	
		Max	Mean
^{11}C	20.4	4.1	1.1
^{13}N	9.96	5.1	1.5
^{15}O	2.03	7.3	2.5
^{18}F	109.8	2.4	0.6

A schematic example of the β^+ decay and subsequent annihilation is shown for the decay of ^{11}C to ^{11}B in **Figure 9**. This figure well represents a summary of the discussed equations of this chapter. The conversion of a proton to a neutron in the $^{11}_{6}C$ nucleus reduces the atomic number by one. Therefore, this is now an $^{11}_{6}O$ atom. The mass number remains untouched, because the total number of particles in the nucleus is the same as before. Moreover, from **Figure 9** it is also apparent that the atom remains charge neutral since the number of electrons in the outermost shell is reduced by one. The left side of the figure shows the positron traveling a short distance from the nucleus and then annihilating with an electron. The emitted photons are drawn as sinusoidal lines.

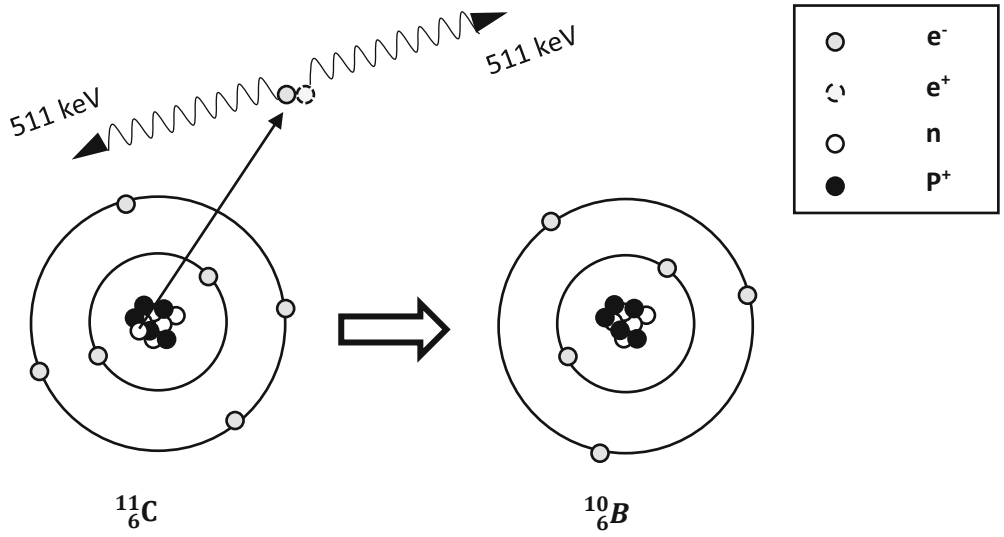

***Figure 9**: β^+ decay of $^{11}_{6}C$ to $^{11}_{5}B$: The created antiparticle annihilates with its counterpart and produces two photons of 511 keV travelling into opposite directions. electron (e^-), positron (e^+), neutron (n), proton (p^+); based on* (Maisey, 2005)

One of the key benefits of PET imaging is its versatility. Changing the used radiotracer allows to investigate a wide range of processes within the living organism. A tracer consists of two essential components. Firstly, typically a molecule that specifically follows a certain physiologic pathway or biochemical process of interest is needed. Once such a tracer is found, it can be labeled with a β^+ emitter (Cherry et al., 2012).

Such a radiotracer should adhere to the following principles. It should allow absolute quantification. The radiolabel must not alter the tracer's properties. The radiotracer should only be administered in trace amounts. Moreover, the tracer should exhibit selectivity to a single pathway, limited peripheral metabolism and plasma binding. In case of neuroimaging with PET, another restriction for applicable PET tracers is that they must be able to cross the blood-brain-barrier (Turkheimer et al., 2014).

One of the most widely known radiotracers is ^{18}F labelled fluorodeoxyglucose, a radiolabeled sugar, that is often applied in order to find areas of high energy demand such as cancer growths and metastases. Other radiotracers that are of special interest in psychiatric research, such as [*carbonyl*-^{11}C]WAY for imaging of the serotonin 5-HT$_{1A}$ receptor, are listed in **Table 2** (Turkheimer et al., 2014).

Table 2: *applications for* selected PET tracers; taken from (Turkheimer et al., 2014)

Tracer	Application
[^{18}F]FDG	glucose metabolism
[^{18}F]F-DOPA	dopamine synthesis
[^{11}C]raclopride	dopamine type 2 receptor
[*carbonyl*-^{11}C]WAY-100635	serotonin 1A receptor
[^{11}C]DASB	serotonin transporter

Since [*carbonyl*-^{11}C]WAY-100635 was used in the PET studies that this thesis builds upon, here is a short overview of the reactions involved in its synthesis (see also **Figure 10**). At first, (^{11}C)CO_2 is produced in a cyclotron via the bombardment of nitrogen gas with protons. The radiolabelled molecule then reacts with cyclohexylmagnesium chloride (see top of figure). The resulting carboxylation adduct is then treated with thionyl chloride ($SOCl_2$), producing [*carbonyl*-^{11}C]cyclohexanecarbonyl chloride (centre of figure). As a final step of the synthesis WAY-100634 is acylated with the product of the previous synthesis step and yields the tracer labelled at the carbonyl position (see right side of **Figure 10**). Purification via high-performance liquid chromatography is required as well (Krasikova et al., 2009).

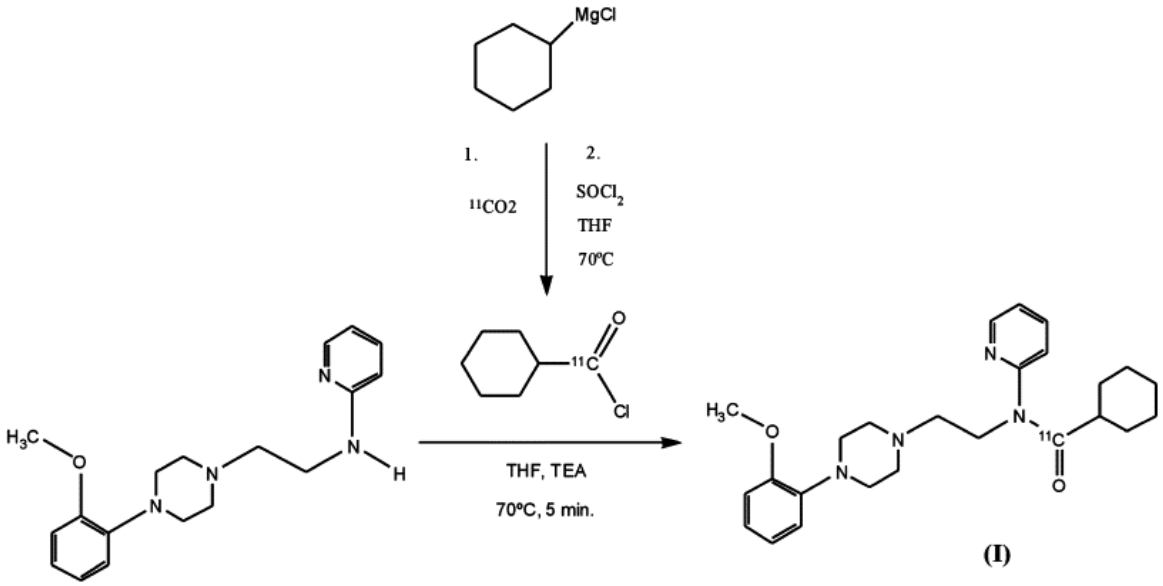

Figure 10: *Synthesis of [carbonyl-^{11}C]WAY-100635; THF: tetrahydrofuran; taken from* (Krasikova et al., 2009)

2.2.2 Detection

As mentioned above, the two photons are created from the annihilation of positron and electron. They travel ideally diametrical from the point of origin, which is in close proximity to the β^+ emitter (for mean paths in water refer to **Table 1**). By placing the emitters into a detector ring, it is possible to detect both photons and it can be deduced that annihilation took place somewhere along the line between the two detected signals (line of response). Evidently, this only holds true for an exact 180° angle between photons and in the absence of scattering. Two signals are assumed to belong to the same annihilation event if they fall within the same coincidence timing window of about six to twelve nanoseconds (Cherry et al., 2012). Figure 11 shows several annihilation events and which of those lead to recorded events in 2-D detection. This mechanism is referred to as annihilation incidence detection (ACD). Another detection mechanism is time-of-flight PET, that requires extremely high temporal resolution (Cherry et al., 2012)

The detector technology in PET scanners typically is based on scintillation (Turkheimer et al., 2014). Other categories of radiation detectors have been developed as well. They include gas chambers or semiconductor detectors, but both perform poorly compared to scintillation detectors when operating at an energy range around 511 keV, which is required for PET (Maisey, 2005).

Scintillating materials release a part of the energy taken up after irradiation as visible light or in the UV spectrum during relaxation of electrons from the conduction band to the valence band (Maisey, 2005). Relevant properties for the selection of scintillators are their intrinsic energy resolution, stopping power for photons at 511 keV, the signal's decay time and light output. Sodium iodide doped with thallium and bismuth germinate ($Bi_4Ge_3O_{12}$) are commonly applied scintillating materials used in PET (Maisey, 2005).

The amount of light resulting from the scintillation emission is proportional to the total energy deposited by the incident radiation. The limitation of only a small amount of light being produced, even for those materials with comparable high light output at the energies of 511 keV or smaller, is overcome by the application of photomultiplier tubes. A typical scintillating detector is a gamma camera. A collimator restricts the angle of incoming photons close to perpendicular with respect to the detector. This is essential for forming a projected image in X-Ray or single photon emission tomography. However, ACD has no need for such absorptive collimation. This results in higher sensitivity compared to technologies that require such collimation (Cherry et al., 2012)

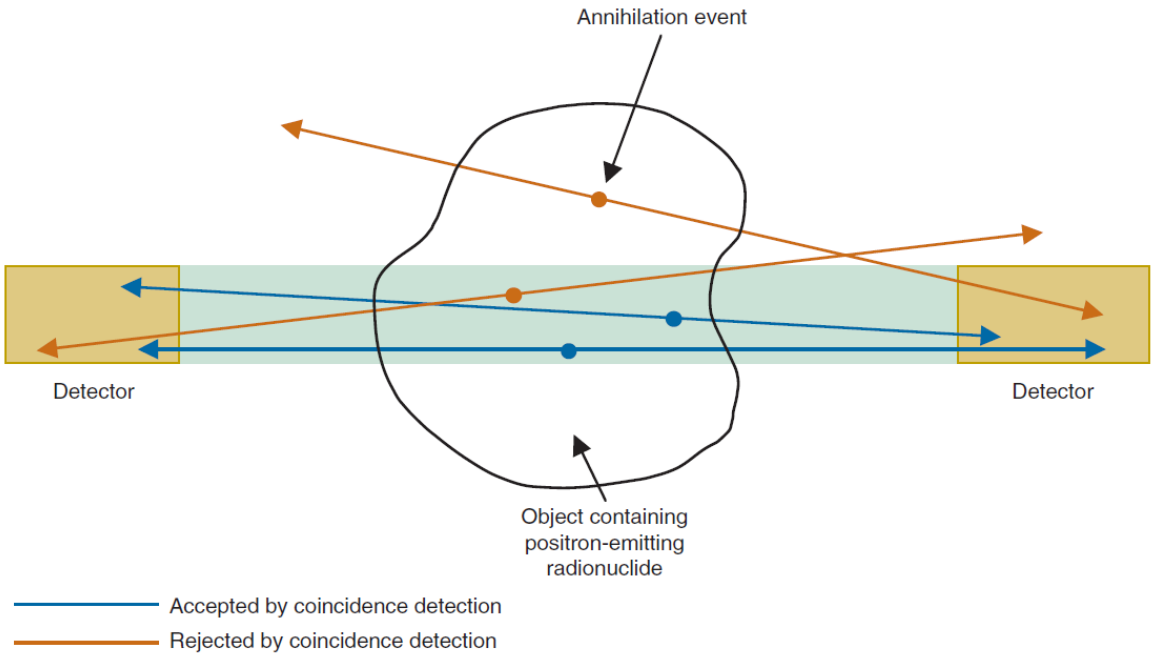

***Figure 11**: PET detection; acceptance and rejection due to coincidence detection; taken from* (Cherry et al., 2012)

2.2.3 Data Correction in PET

The goal in PET imaging is to obtain intensities in the reconstructed voxels that are proportional to the concentration of activity in the corresponding body regions. In order to achieve this, several corrections are required after acquisition. The most common corrections account for random events, dead time, scatter and tissue attenuation (Cherry et al., 2012; Turkheimer et al., 2014).

As mentioned in **Section 2.2.2**, two incident photons are assumed to originate from the same annihilation event if they are detected within a coincidence timing window. Besides true incidences, it is also possible that photons from different, unrelated annihilation events fall within the same coincidence timing window. These random coincidences add an approximately random background to the image. As a result, contrast will be decreased and the actual relationship between amount of activity and intensity is distorted (Cherry et al., 2012). Several methods for correction of random coincidence exist. One such approach is tail fitting. If the object of interest only occupies a part of the field of view, the volume outside the FOV can be used to fit a Gaussian function. A more elaborate approach uses delayed coincidence estimation. Additionally, to the original timing signal, a delayed duplicate data stream is recorded. The delay is in the order of several times the

coincidence window. The delayed data can only produce random coincidences. This can be used to estimate the random events and subtract them from the original data (Meikle & Badawi, 2005).

Similar to random coincidence, scattering reduces the image contrast and affects the relationship between activity and intensity. However, unlike random coincidence, scattering is not uniformly distributed but concentrated on the image centre. In 3-D imaging of the abdomen, where scattering has a very strong impact, the fraction of scattered photons can be in the range of 60 to 70%. An aspect contributing to the issue is, that at 511 keV scattering is the dominant interaction in scintillators. Scatter events in body and in the scintillator cannot be distinguished (Cherry et al., 2012). A variety of approaches exists to reduce the impact of scattered photons in PET imaging. Events that lie on a line of response outside the object can be assumed to be a result of scattering, if the data has already been corrected for random events. Moreover, similar to the correction for random coincidence, an analytical function can be fitted to the scatter tails outside the body. Other approaches estimate the contribution of scattered photons by using multiple energy windows or perform numerical simulations (e.g. Monte Carlo techniques) (Meikle & Badawi, 2005).

The scintillation detectors emit photons upon electronic relaxation after electrons are excited by incoming radiation. If the decay to the ground state is too slow or too many annihilation photons are incident, the detector cannot respond (i.e. is saturated). The non-linear response of the detector when it is close to saturation is referred to as dead time (Turkheimer et al., 2014). A simple procedure that many scanners use in order to deal with dead time are empirical dead time models (Cherry et al., 2012; Meikle & Badawi, 2005).

Attenuation correction is considered to be the most important correction in PET. Assuming an annihilation takes place at depth (x) within an object with thickness (T), **Eq. (7)** describes the probability (P_{det}), that both photons reach a detector pair. The product of the individual probabilities is independent of x and only increases with the thickness of the object. μ is the linear attenuation coefficient in tissue (Meikle & Badawi, 2005). Attenuation correction is performed by first measuring an attenuation map. In PET-CT systems a low dose CT scan can be performed. In standalone PET, a γ-ray source may be used to obtain the attenuation map and derive the correction factor for each detector pair (Turkheimer et al., 2014). A recent evaluation of attenuation correction methods for neurotransmitter studies showed the effect on quantification of BP_{ND}. An approach based on T1 weighted MRI data that is co-registered to a database of CT images was shown to be a suitable alternative to conventional attenuation correction using CT (Rischka et al., 2019).

$$P_{det} = e^{-\mu x} e^{-\mu(T-x)} = e^{-\mu T} \qquad (7)$$

2.2.4 Dosimetry

Exposure to ionising radiation may cause adverse health effects. Therefore, exposing patients to ionising radiation during treatment or imaging needs to be handled with care. It is a trade-off between high-enough dose for achieving satisfactory diagnostic or therapeutic results and keeping exposure as low as reasonable possible to minimise risk. Thus quantifying the distribution of radiation in the body plays a crucial role (Cherry et al., 2012).

Several measures have been introduced concerning the quantification of exposure to radiation. Absorbed dose (D) is the ratio of amount of radiation energy that is absorbed per mass of the absorber. The unit is gray (1 Gy = 1 J/kg). Another dose measure takes the type of radiation into account and is referred to as equivalent dose (H). The reasoning for this is that the interaction of tissue and radiation and thus the amount of energy that is deposited in the absorber, depends on the type of radiation. However, for x-rays, γ-rays, electrons and positrons, the radiation specific weighting factor is equal to one and equivalent dose has the same numeric value as the absorbed dose. Sievert (Sv) has been introduced as the unit of the equivalent dose. Finally, effective dose (E) represents the equivalent dose with an additional weighting factor for each organ. The weighting factor represents the organs' susceptibility to potential damage caused by radiation (Towson, 2005). **Table 3** gives an overview of the discussed dose measures, their units and how they relate to each other.

***Table 3**: overview of commonly used measures in the quantification of radiation dose delivered to tissue; radiation weighting factor (w_R); tissue weighting factor (w_T)*

quantity	equation	unit
absorbed dose (D)	$D = W/m$	Gy
equivalent dose (H)	$H = D\, w_R$	Sv
effective dose (E)	$E = H\, w_T$	Sv

Dose is not monitored for each patient in clinical practice. Rather the dose delivered to specific organs and the whole body is calculated from the administered radionuclides. One such method is the Medical Internal Radiation Dosimetry (MIRD) formalism. Organs are referred to in terms of source and target. The former contains radioactive material and for the latter the dose due to emission from source organs is calculated (Bushberg et al., 2012).

The radiation dose that is delivered to the target organ depends among other factors on the cumulated activity ($\tilde{A}$) in the source organs. It can be described as the area under the time activity curve or in other words the time integral of the activity and corresponds to the total amount of radioactive disintegrations. The amount of energy emitted by radiation from a source region is described by the equilibrium absorbed dose constant (Δ). Furthermore, the absorbed fraction (Φ) gives the fraction of energy that is emitted by the source and then absorbed by the target. It depends on the type of radiation, its energy and the anatomical relations between organs (Cherry et al., 2012). **Eq. (8)** relates the above mentioned parameters to the average absorbed dose to the target (r_T) from emission in all source organs (r_S). While the cumulated activity and the equilibrium absorbed dose constant are well characterised by the radionuclide, the absorbed fraction relies on estimates of organs masses and their relative positions to each other. Based on the original MIRD model (Snyder et al., 1978), adjustments to the estimated parameters have been made to account for juvenile bodies (Cristy & Eckerman, 1987) and models for women and pregnant women are available as well (Stabin et al., 1995).

$$\bar{D}(r_T \leftarrow r_S) = \frac{\tilde{A}}{m_t} \sum_i \Phi_i(r_T \leftarrow r_S)\Delta_i \qquad (8)$$

Recommended dose limits have been introduced by the International Commission on Radiological Protection (ICRP). A distinction is made between occupational and public exposure. For the former, a maximum effective dose of 20 mSv per year is recommended whereas for the wider public a value of 1 mSv is given (Sutton et al., 2014). Effective dose resulting from a PET scan depends on the radionuclide and exact protocol. For PET scans, effective doses of 0.015 mSv/MBq (Parsey et al., 2005) and 0.019 mSv/MBq (Towson, 2005) have been reported in studies using [*carbonyl*-^{11}C]WAY-100635 and [^{18}F]FDG, respectively.

2.3 Preprocessing

The raw imaging data as acquired by the scanner during PET or MRI studies is not yet suitable for extracting properties of interest or interpatient comparisons. Generally, preprocessing is needed to reduce artefacts, increase image quality and transfer scans of individuals to a normalised space (Friston et al., 1995). These tasks generally require matching one image to another. Examples include matching a time series to a representative image of itself, matching data from different modalities such as MRI and PET (Friston, 2004), or matching imaging data to a template. Methods for image

registration include landmark based and voxel-based methods (Turkheimer et al., 2014). In this section, only a short look at voxel-based methods is presented.
At the core of voxel-based image registration, lies an algorithm that tries to maximise or minimise a cost function (Friston, 2004). The target of the cost function should be a parameter that describes how well one image matches the other. This is a rather general description, but except for a schematic overview of the involved topics, a more detailed discussion is beyond the scope of this thesis.

Relevant termini for registration are source and reference. The source represents the image that will be transformed to match the reference image. In the case of imaging data obtained from the same patient with the same modality, the target of the cost function can be rather simple. A rigid body transformation that iteratively minimises the sum of squared differences between the images will work (Turkheimer et al., 2014). A closer look at rigid body transformation can be found in **Section 3.3**. For between-modality registration (e.g. PET to T1 weighted MRI), however, intensities between images show no linear relationship (Friston, 2004).

Several measures were developed that try to deal with the issue of intermodal registration. These measures include entropy or more relevant today, (normalised) mutual information (MI) and are generally based on probability distributions of intensities in the images (Friston, 2004). MI of corresponding voxel intensities can be seen as a measure of information about one image that is contained in the other image. Assuming that we find a maximum of MI when the two images are properly aligned, we see that mutual information is an adequate target for a cost function (Maes et al., 2015).

Even though, a PET scan and a T1 weighted MRI scan contain different information (i.e. functional and structural), the intensity values at corresponding points still are not completely independent observations but actually statistically related. In **Eq. (9)** MI is expressed as a function of joint (p_{AB}) and marginal (p_A and p_B) probability distributions. With respect to p_{AB} it is useful to first establish the idea of joint histograms. A joint histogram is constructed from the intensities of two images A and B. For each voxel in image A its intensity (a) is plotted against intensity b in image B at the corresponding voxel location. Therefore, each value in the joint histogram corresponds to the counts of voxels with intensity a in A and b in B. Intensity pairs that occur more often are displayed brighter (Hill et al., 2001). The leftmost image in **Figure 12 (a)** shows the trivial case of a joint histogram of a MR image with itself. Other, more relevant examples of registration are also provided. For all examples in **Figure 12**, characteristic blurring is seen upon shifting one image away from the position of perfect alignment and then calculating the joint histogram.

Issues that may arise are that the number of voxels is not the same or that one image has more intensity bins than the other does. To deal with different number of voxels, the original voxels are interpolated in order to obtain the intensity at the new voxel locations. The interpolation can be performed by several methods, such as nearest neighbor, linear or higher-order interpolation (Turkheimer et al., 2014).

The joint probability distribution (p_{AB}) can be obtained from the joint histogram by dividing each value h(a,b) by the total number of voxels. p_A and p_B are also obtained from the normalised joint histogram by the projection onto the respective axes. MI can be

expressed as a function of these probability distributions (see **Eq. (9)**). If the intensities in images A and B are independent of each other p_{AB} equals the product of the marginal probability distributions and we find a minimum of MI at zero. The other extreme is found by a one-to-one mapping where $p_A(a) = p_B(b) = p_{AB}(a, b)$.

$$MI(A, B) = \sum_{a,b} p_{AB}(a, b)\ log \frac{p_{AB}(a, b)}{p_A(a)\ p_B(b)} \qquad (9)$$

In order to fully establish the relevance of MI for image registration the transformation of one image needs to be considered. After calculating MI the transformation T is applied to the source (e.g. image B). Afterwards MI can be calculated anew. These steps are iteratively performed until a maximum is obtained. Typically used algorithms include gradient descent, Powell's method, or simplex search (Maes et al., 2015).

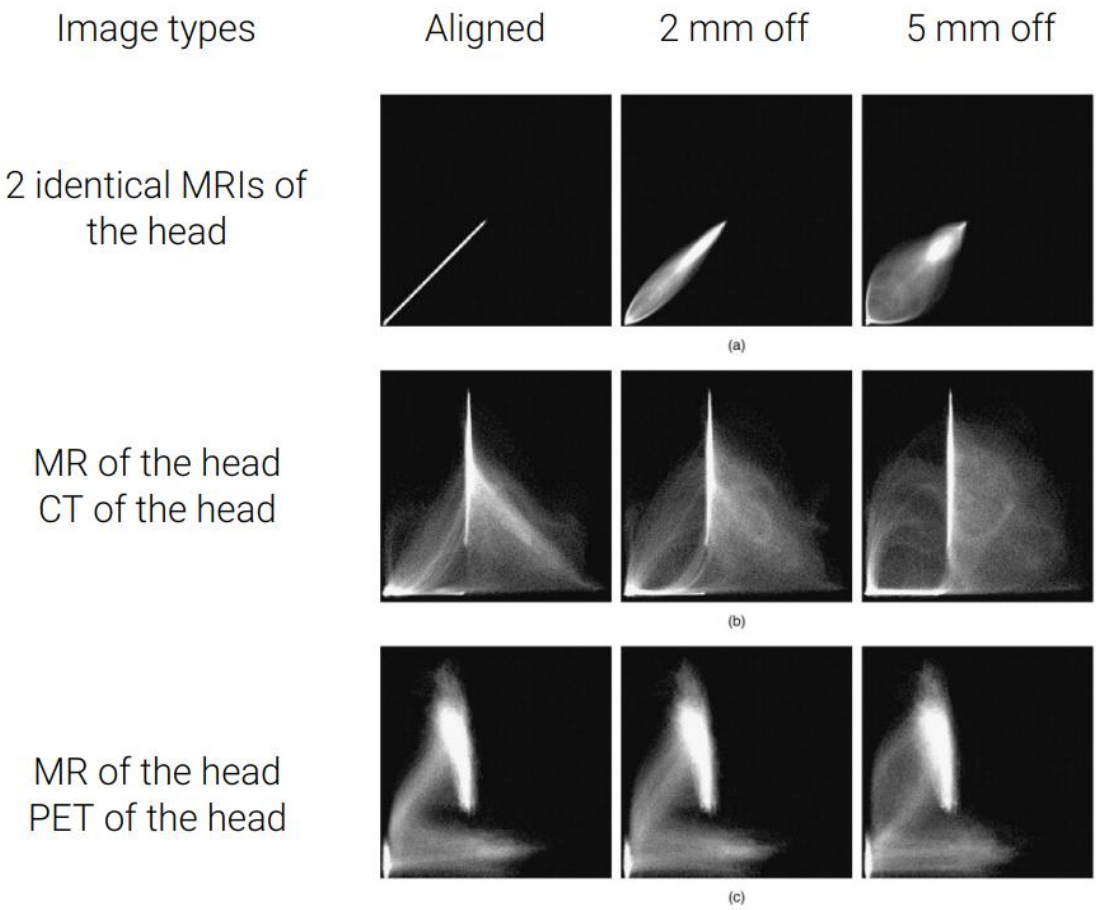

Figure 12: *joint histograms of different image types and varying degrees of misalignment; Images are shown for aligned data and after translation of 2 and 5 mm for identical MRIs* ***(a)****, MRI and CT* ***(b)****, MRI and PET* ***(c)****; taken from* (Hill et al., 2001)

2.4 Kinetic Modelling

After preprocessing, quantification typically is the next step in a PET study. Methods with and without arterial blood sampling have been introduced. The latter (noninvasive) approach includes image-derived input function and kinetic modelling (Turkheimer et al., 2014). In this section a closer look at the kinetic modelling will be presented.

After the tracer is administered, it is transported in the blood plasma to the tissue. Based on that, we see that the tracer is present in different forms: in plasma, free in tissue, specifically bound in tissue and non-specifically bound in tissue. Rate constants (k) are used to describe the transition between these conditions (Turkheimer et al., 2014).

When assuming that the free tracer in tissue and non-specifically bound tracer quickly equilibrate, they can be combined to a single compartment. It represents the non-displaceable tracer fraction (C_{ND}). Since we are looking at two compartments within the tissue and three compartments in total, this model is referred to as two-tissue compartment model or three compartment model. If the nondisplaceable fraction and specifically bound fraction cannot be kinetically distinguished or the region is receptor-less a one-tissue compartment model is the result. **Figure 13** visualises the concepts of one- and two tissue compartment models. Based on these models and the imaging data from PET, the macro-parameters to quantify the receptor density can be derived (Turkheimer et al., 2014).

The parameters of interest are distribution volumes (V) and binding potential (BP). V is given as the ratio of ligand concentration in a certain compartment to the total plasma activity at equilibrium (Turkheimer et al., 2014). Another way to phrase this is that V refers to the amount of plasma required to account for the total amount of radioligand in a unit-volume of a certain compartment (Innis et al., 2007). Three distribution volumes can be defined: total (V_T), nondisplaceable (V_{ND}) and specific (V_S) (Turkheimer et al., 2014).

BP is the ratio of specifically bound tracer concentration to concentration in a certain compartment at equilibrium. Similar to the volume of distribution also BP can be defined for the nondisplaceable fraction (BP_{ND}) and fraction in plasma (BP_P) (Turkheimer et al., 2014). Below in **Eq. (10)** and **(11)** the mathematical descriptions of total volume of distribution and nondisplaceable binding potential are given. They also show that besides the definitions given above, those parameters can also be explained via the rate constants.

Reference tissue models are used to estimate BP without blood sampling. The assumption is that a region with little to no specific receptor binding exists. This region is used to model the receptor binding in other regions (Hirvonen et al., 2007).

$$V_T = \frac{C_T}{C_P} = \frac{C_{ND} + C_S}{C_P} = \frac{k_1}{k_2}\left(1 + \frac{k_3}{k_4}\right) \quad (10)$$

$$BP_{ND} = \frac{C_S}{C_{ND}} = \frac{k_3}{k_4} \quad (11)$$

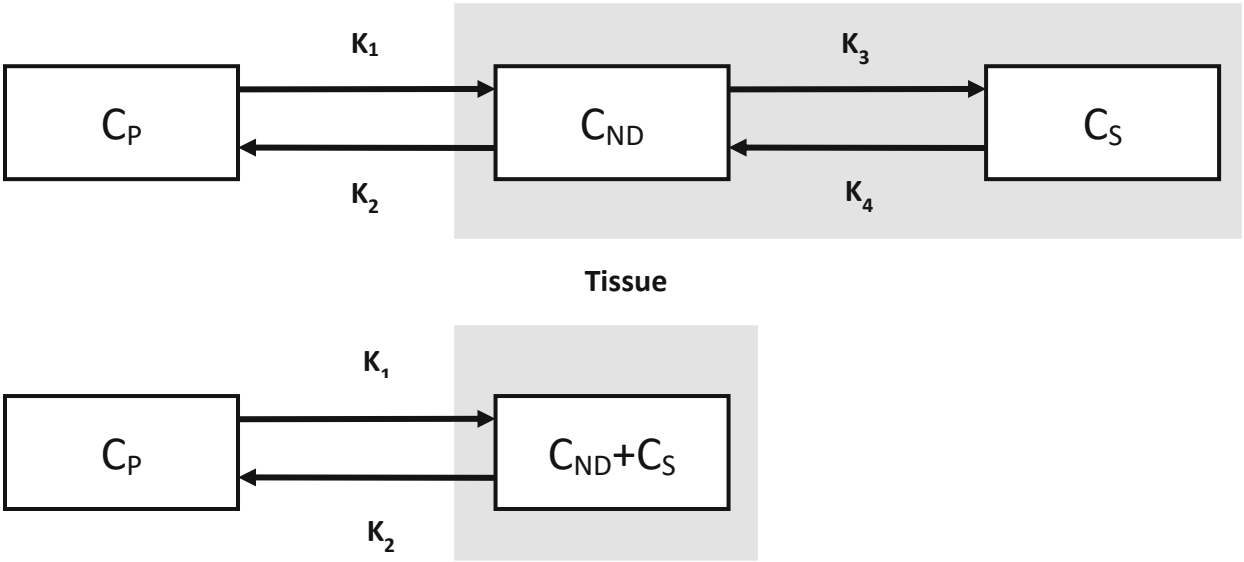

Figure 13: *one- and two-tissue compartment models; Rate constants (k) describe the transition of tracer between the compartments. Tissue compartments are drawn within a grey box. adapted from* (Turkheimer et al., 2014)

Ichise et al. developed a multilinear reference tissue model ($MRTM_0$) and further refined it into the models MRTM and MRTM2 (Ichise et al., 1996, 2003). This section gives a brief overview of the operational equations and reasoning for the changes applied to $MRTM_0$.

The operational equation for the original model can be found in **Eq. (12).** In this section a parameter marked with an apostrophe refers to the property of the reference tissue and lack thereof to tissue (i.e., C(t) and C(t)' are the total distribution volumes of tissue and reference tissue respectively). V is the voxel time-radioactivity concertation in kBq/ml and b is the intercept term. **Eq. (12)** can be rearranged to **Eq. (13).** This step eliminates the noisy variable C(T) from the dependent variables (left side of equation). The presence of C(T) in the integral is tolerated because integrals of noisy variables show smaller variations then the original variables. This yields the MRTM (see **Eq. (13)**). For

this model three parameters are estimated by ordinary least squares estimation. The parameters are $\gamma_1 = -V/(V'b), \gamma_2 = 1/b, \gamma_3 = -V/(V'k_2'b)$.

$$\frac{\int_0^T C(t)dt}{C(T)} = \frac{V}{V'}\int_0^T \frac{C'(t)dt}{C(T)} + \frac{V}{V'k'}\frac{C'(T)}{C(T)} + b \qquad (12)$$

$$C(T) = -\frac{V}{V'b}\int_0^T C'(t)dt + \frac{1}{b}\int_0^T C(t)dt - \frac{V}{V'k'}\frac{C'(T)}{C(T)} \qquad (13)$$

$$C(t) = -\frac{V}{V'b}\left(\int_0^T C'(t)dt + \frac{1}{k_2'}C'(T)\right) + \frac{1}{b}\int_0^T C(t)dt \qquad (14)$$

$$BP_{ND} = \frac{V_T}{V_T'} - 1 = -\left(\frac{\gamma_1}{\gamma_2} + 1\right) \qquad (15)$$

If **Eq. *(13)*** is used as a preliminary step to estimate k'$_2$, and then the equation is rearranged, we arrive at the two-parameter version MRTM2 (see **Eq. *(14)***). For this model the estimated parameters are $\gamma_1 = -V/(V'b)$ and $\gamma_2 = 1/b$. From these two regressors BP$_{ND}$ can be derived as $BP_{ND} = -(\frac{\gamma_1}{\gamma_2} + 1)$. It can be reasoned that the removal of the noisy tissue radioactivity term and reduction of the estimated parameters to just two, provide reduced variability in the estimation of B P$_{ND}$ and stable parametric images (Ichise et al., 2003).

Figure 14 shows a visualisation of the BP$_{ND}$ that was modelled with MRTM2. Areas of higher binding potential in frontal and temporal regions are drawn in red. The cerebellum is usually assumed to be devoid of 5-HT$_{1A}$ receptor (Hirvonen et al., 2007).

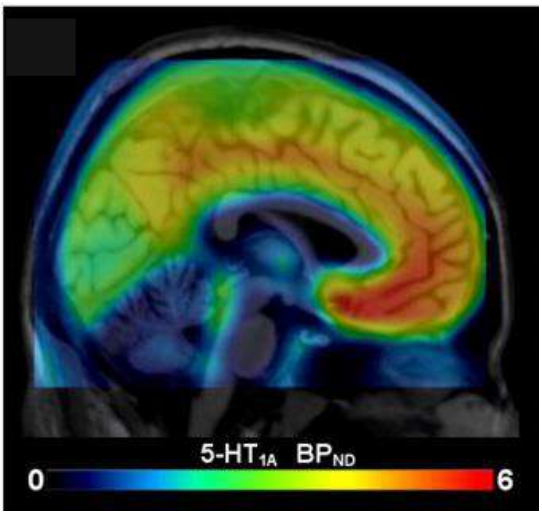

***Figure 14**: averaged non-displaceable binding potential (BP_{ND}) for the 5-HT_{1A} receptor in the human brain; BP_{ND} was modelled with the MRTM2. taken from* (Savli et al., 2012)

3 Methods

This analysis represents a cross-sectional study of a healthy control and a TRD subject group. All data were acquired and kindly provided by the Neuroimaging Labs (NIL, head: Prof. PD Dr. Rupert Lanzenberger), Department of Psychiatry and Psychotherapy, Medical University of Vienna, Austria.

3.1 Study Participants

A total of 40 subjects were selected for analysis, with equal numbers in patient and control group ($n_{TRD} = 20$, $n_{HC} = 20$). The subjects for the control group were selected from two separate studies. 17 and 3 subjects were selected respectively from (Lanzenberger et al., 2007) and (Baldinger et al., 2014) for the total of 20 subjects. The subjects for the TRD group all came from the same study.

An overview, including sex, mean age and standard deviation of age, is shown in **Table 4**. Chi-squared and Student t's t-tests showed that age and sex where independent of group membership. (both > 0.5)

3.2 Data Acquisition

For all subjects, the radioligand [*carbonyl*-^{11}C]WAY-100635 was injected intravenously, and PET data was acquired over an interval of 90 minutes. A structural T1 weighted MRI scan was performed as well. Data acquisition was uniform for the TRD subjects, but two different frame timings were used for the control group. For the treatment resistant group at total of 51 volumes were acquired. In the case of the healthy controls, one subgroup had 30 volumes and the other 50. The differing acquisition parameters are owed to the fact that the data is pooled from three distinct studies. A more detailed look at the frame timings is given in **Table 5**.

An overview of the processing and analysis steps is shown in **Figure 15**. The two main blocks are the pre-processing of the imaging data and the statistical analysis. Pre-processing for the TRD dataset was not performed during the course of this master thesis. Data was processed by Matej Murgaš, MMSc. of the NIL until spatial normalization. Nevertheless, both datasets where pre-processed in the same way.

Table 4: descriptive statistics for TRD subjects and healthy controls; standard deviation (sd)

group	female	male	mean age	sd age
TRD	9	11	28.95	5.18
HC	10	10	33.25	8.23

Table 5*: acquisition times for PET imaging; Number of acquired frames with given timing are displayed for TRD group and the two HC groups (HC1, HC2). Total acquisition time was 90 minutes for all subjects.*

	group		
duration (s)	TRD	HC1	HC2
5	12	0	12
10	6	0	6
20	3	0	3
30	6	0	6
60	9	15	4
120	0	0	5
300	15	15	14

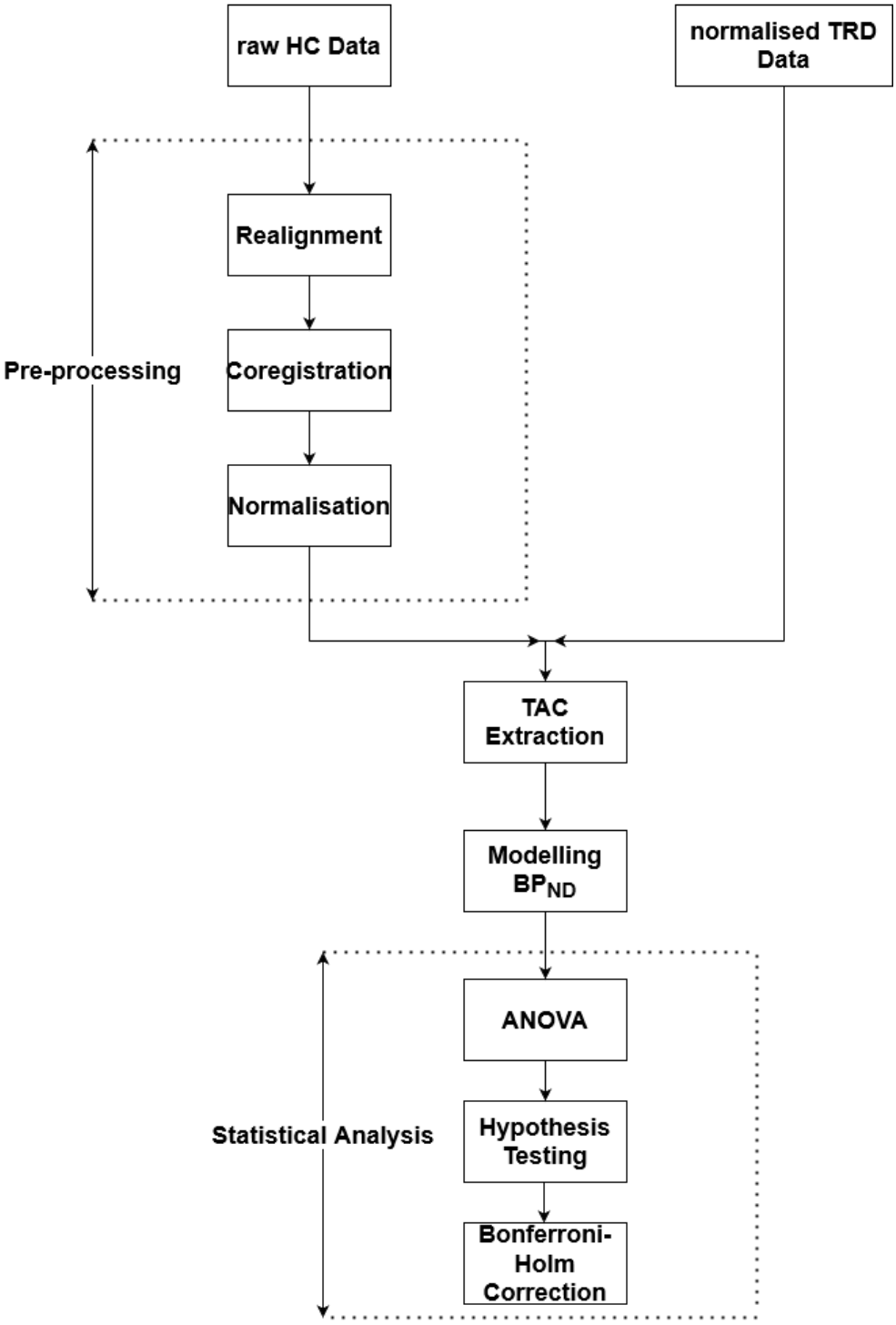

***Figure 15**: Overview of processing and analysis steps; Pre-processing included the same steps for TRD and HC data but was performed by different individuals.*

3.3 Pre-processing

Firstly, MRI data was uniformly oriented, and the origin of MRI and PET data were set. Both steps ensure faster and overall better performance in co-registration and normalisation.

For reorienting the structural MRI data, each image was reviewed. For this as well as the following processing steps, the functions provided by the statistical parametric mapping tool SPM12 (The Wellcome Centre for Human Neuroimaging, www.fil.ion.ucl.ac.uk) in combination with MATLAB version 2018b (The Math Works Inc., www.mathworks.com) were used. More precisely the 'spm_check_registration' function was applied in a script iterating over all MRI files. The reasons why this procedure was chosen over other tools such as MRIcro were twofold. Firstly, the SPM12 visualisation tools read the header of the NIfTI files. This is of special interest for the purpose of checking the orientation of the images since the header may contain transformations. Secondly, maybe less important when using SPM12 in MATLAB the process of opening each file can be automated, minimising the risk of opening the wrong file and thus possibly mislabelling the orientation of a file.

Below, a simplified and condensed version of the code used to reorient the NIfTI files can be found. It shows how a NIfTI file is loaded and an array of zeros in the same x, y, and z dimensions is created. Since the images need to be mirrored along the x-z-plane the script iterates over the number of x-z-planes of the original image and exchanges them with the corresponding mirrored x-z-planes (e.g. first plane with last, second with second-to-last and so on). Based on the obtained array, functions from MATLAB toolbox 'Tools for NIfTI and ANALYZE image' (Shen, 2022) were used to create a MATLAB structure of the same form as the original and subsequently generate a NIfTI file from it.

```
img = load_nii(T1.nii);
imgFlipped = zeros(T1.hdr.dime.dim(2:5));
for y = 1:nrOfRows
     imgFlipped(:,y,:) = img.img(:,end+1-y,:);
end
nii = make_nii(imgFlipped);
save_nii(nii, reorientetT1)
```

After setting a uniform picture orientation, the graphical user interface that is accessed via 'spm_image' was used to set the origin of both, MR and PET images to the same anatomical structure. Since the PET data consisted of several volumes and the first few volumes show little to no recognisable landmarks, volume number fifteen was generally used to set the origin. The coordinates were then applied to the remaining volumes of the respective PET scan.

Using SPM12, the data was then realigned. During realignment, movement-induced changes in the voxel time-series are reduced (Frackowiak et al., 2004). Basically, the volumes of the time series are registered to either a chosen volume of the same time series or a mean image thereof. The realignment performs a six parameter (three rotations and three translations) rigid body transformation using a least squares approach. A possible formulation of such a transform is described in **Eq. (16) - (18),** where **x** and **y** denote the image before and after transformation respectively (Friston, 2004). It can be seen that the rotation and translation matrices are simply combined by multiplication. The parameters q_1 through q_3 are the translations along x, y and z respectively. The other three parameters are the rotations about x, y and z (or pitch, roll and yaw) given in radians. The six estimated parameters are saved to the header file.

The advantage of this formalism is that additional transformations are easily added to the already existing ones. Consequently, the images generally do not need to be resliced between processing steps which avoids unnecessary interpolations, unless the intermediate output is required.

With reference to **Section 2.3** we can look at the realignment in the following way. The source images are the acquired volumes, and the reference is the mean image. Following the notation of **Eq. (9)**, mutual information of source (**A**) and reference (**B**) is calculated. After each iteration, **A** is updated in the following way: $\boldsymbol{A = MB}$ (see also **Eq. (18)**).

The PET data was realigned to the mean image of the movement free slices defined by visual inspection. Information on the movement free slices was provided alongside the imaging data and did not have to be determined during the work for this thesis. The quality property was set to 1, for a more precise result then the default 0.9 at the cost of slower realignment. Moreover, the data was resliced as well, which applies the estimated parameters of the rigid body transform in addition to just writing them to the header. This was needed, because for the subsequent co-registration, a weighted mean of the realigned PET images was calculated. For interpolation (see also **Section 2.3**), 4th degree B-spline were used.

$$\boldsymbol{T} = \begin{pmatrix} 1 & 0 & 0 & q_1 \\ 0 & 1 & 0 & q_2 \\ 0 & 0 & 1 & q_3 \\ 0 & 0 & 0 & 1 \end{pmatrix} \qquad (16)$$

$$\boldsymbol{R_x} = \begin{pmatrix} 1 & 0 & 0 & 0 \\ 0 & \cos(q_4) & \cos(q_4 & 0 \\ 0 & -\sin(q_4) & \cos(q_4) & 0 \\ 0 & 0 & 0 & 1 \end{pmatrix}$$

$$\boldsymbol{R_y} = \begin{pmatrix} \cos(q_5) & 0 & \sin(q_5) & 0 \\ 0 & 1 & 0 & 0 \\ -\sin(q_5) & 0 & \cos(q_5) & 0 \\ 0 & 0 & 0 & 1 \end{pmatrix}$$

$$\boldsymbol{R_z} = \begin{pmatrix} \cos(q_6) & \sin(q_6) & 0 & 0 \\ -sin(q_6) & cos(q_6) & 0 & 0 \\ 0 & 0 & 1 & 0 \\ 0 & 0 & 0 & 1 \end{pmatrix}$$

$$\boldsymbol{R} = \boldsymbol{R_x R_y R_z} \quad (17)$$

$$\boldsymbol{A} = \boldsymbol{MB} = \boldsymbol{TRB} \quad (18)$$

The realigned PET data was subsequently co-registered to the T1 weighted scan of higher resolution. As was the case for the realignment, co-registration estimates six parameters for the three-dimensional rigid-body transformation.

Co-registration performs the task of bringing the physiologic (PET) data into alignment with the structural information found in MRI scans. It is as mentioned earlier, a registration of the PET images to the MRI scan. In accordance with the terminology used earlier for image registration, the PET data represents the source and the MRI image the reference. SPM12 uses an algorithm based on work by Collignon et al. (Collignon et al., 1995). The original voxel similarity-based registration algorithm has been adapted for SPM12. It adds additional smoothing to images and histograms. The changes provide a smoother cost function and faster convergence (Ashburner et al., 2021).

Since not all acquired volumes of the PET scans were acquired over the same time, a weighted mean was used as the source image for co-registration, meaning that the transformation parameters were estimated for the mean image and applied to all volumes. Weights (w_i) were determined by the ratio of acquisition time of a single volume (d_i) to total scan time (see **Eq. (19)**). The equation was implemented with the 'spm_imcalc' function, allowing to address the acquired volumes without having to manually load the data. Normalised mutual information was used as the objective function. The estimated parameters were then applied to the realigned PET data. Once again, the co-registered data was resliced, using 4th degree B-spline for interpolation.

$$w_i = \frac{d_i}{\sum_i^n d_i} \quad (19)$$

In the next step, the T1 image and PET scans were normalised. The normalisation represents another special case of image registration. During normalisation the source is brought into a standard space. This enables identification of e.g. binding sites across subjects. The standard MNI-space provided by SPM12 was used. The algorithm for

normalisation is based on the method described by Ashburner and Friston (Ashburner & Friston, 2005). Changes from the original approach include use of an improved registration model and a different treatment of mixing proportions (Ashburner et al., 2021).

The transformation parameters were estimated by the structural image and applied to both the MRI and co-registered PET data. The same transformation can be applied to the PET scan because the coordinates in the PET data correspond to those of the MRI scan due to the co-registration. The ICBM space template for European brains was chosen for the affine regularisation parameter.

After the pre-processing, the normalised MRI and PET data were displayed alongside the tissue probability map that was used for normalisation. This showed any obvious failures in either realignment, co-registration or normalisation. For subjects where the pre-processing did not produce satisfactory results, the parameters for the pre-processing step of interest were adjusted and the results re-analysed.

3.4 Modelling BP_{ND}

Following the pre-processing, the BP_{ND} was modelled for TRD and HC groups. Using [*carbonyl*-^{11}C]WAY-100635, cerebellar white matter (CWM) has been found to be a suitable reference region devoid of 5-HT_{1A} receptors, which is a requirement for modelling specific with a reference tissue model (Hirvonen et al., 2007).

For the modelling, time activity curves (TACs) were extracted for each subject from insula and cerebellar white matter (CWM) for each acquired volume in the time series. An in-house atlas (Savli et al., 2012) was used to calculate the mean activity for each acquired volume. The code seen below, shows how the mean values were extracted from the two regions. After loading the NIfTI file of the normalised PET data with the 'load_nii' function, the created structure contained a four-dimensional array with dimensions corresponding to the number of voxels in x, y and z direction and the number of acquired volumes. The code below iterates over the number of images in the time series and creates a mean that ignores NaN values and zeros. Voxels containing Insula are labelled with 1 and those containing CWM are labelled with 2. Logical indexing was used to address the corresponding voxels in a concise manner.

```
for t = 1:nr_vol
     vol = my_img.img(:,:,:,t);
     tacIns(t) = nanmean(nonzeros(vol(atlas.img == 1)),'all');
     tacCWM(t) = nanmean(nonzeros(vol(atlas.img == 2)),'all');
end
```

The obtained mean values were written to a table and saved with a '.tac' file extensions, so that the modelling software could interpret them in a later step. Moreover, while the TAC extraction was performed the same way for all subjects, three cases had to be distinguished to add the correct acquisition times to each file.

The software used for modelling was PMOD (PMOD Technologies LLC, https://www.pmod.com/web/) version 3.5. PMOD's implementation of Ichise's MRTM2 model was applied to estimate the BP_{ND} based on the extracted time activity curves from cerebellar white matter and insula without an arterial input function. The expressions for the operational equation and the BP_{ND} are **Eq.** ***(14)*** and ***(15)*** in **Section 2.4**, where the model is discussed in more detail.

Acquisition time had to be manually selected in correspondence to the acquisition protocol, which was applied for the respective scans. For patient and healthy control subjects the three different frame timings were used with 30, 50 and 51 acquired volumes (**Table 5**). For the receptor-rich region, the subjects' TAC of combined right and left insula were chosen. The TAC of CWM was selected for the receptor-less region. These two regions served for the estimation of k'_2 with MRTM0, which was fixed for the other regions in MRTM2.

After visual inspection of the modelled TAC and a plausibility check for BP_{ND} and k'_2, the model was calculated. Again, BP_{ND} was inspected for plausibility.

Then five regions of interest were defined based on a paper on the 5-HT_{1A} receptor in relation to electroconvulsive therapy in major depression (Lanzenberger et al., 2013). Hippocampus, orbitofrontal cortex (OFC), anterior cingulate cortex (ACC), amygdala and insula were chosen for the statistical analysis.

3.5 Statistical Analysis

The aim of the statistical analysis was to establish whether a significant difference between HC and patient group existed with regard to BP_{ND} in the five ROIs.

To reduce variability in the modelled BP_{ND} that is caused by the subjects belonging to different studies, the MATLAB implementation of ComBat was used. ComBat was originally introduced to reduce non-biological effects in microarray studies that use data from different sites. It can reduce these between-scanner variations not only in the imaging data itself but also in variables derived from those. At its core, ComBat is based on the residuals harmonisation method with site-specific scaling factors and empirical Bayes (Fortin et al., 2017, 2018; Johnson et al., 2007).

Below, the straight-forward function call used in MATLAB is shown. The harmonised data is written to a new variable 'data_harmonised' and the only input arguments are the data to be harmonised (BP_{ND} in variable 'data'), information on study membership and the optional parameter 'mod'. The latter contained information on age and sex. By using this optional input, ComBat attempts to conserve variability caused by these biological factors and remove only the unwanted study-specific variability. For the categorical

variable (sex) a reference group had to be omitted. Women were arbitrarily selected as the reference group. The continuous variable could be used without further modifications. The harmonised data was used for all following analysis steps.

```
data_harmonised = combat(data, study, mod,1);
```

IBM SPSS Statistics 26 (IBM Corp., https://www.ibm.com/spss) was used for the further statistical analysis. The aim was to perform a repeated measures analysis of variance (ANOVA) with the BP_{ND} as the within-subject variable. Five levels for the BP_{ND} were set, corresponding to the regions of interest. Group was used as the between-subject factor. To this end, the necessary conditions for the repeated measures ANOVA had to be checked for validity. A Shapiro-Wilk Test was used to assess normal distribution of BP_{ND} in the five ROIs for patient and control group. Sphericity was evaluated with Mauchly's sphericity test.

After the repeated measures ANOVA, post-hoc tests for the significant effects were performed. The aim was to evaluate the Null hypothesis of equal means between groups. The conditions for a two-sample t-test were evaluated. As before, the Shapiro Wilk test was used for the assumption of normal distribution. Homoscedasticity was evaluated with the Levene's test.

4 Results

4.1 Pre-processing

Visual inspection of the sagittal view easily showed whether anterior-posterior orientation was flipped. An example of the two different orientations is shown in **Figure 16**. **Figure 16** (**b)** depicts the orientation to which all scans were brought (left = posterior, right = anterior), whereas **Figure 16** (**b)** depicts the AP-flipped version. In T1 weighted scans, the orientation is easily checked in the sagittal view of the brain because anatomical structures are clearly visible. For example, the cerebellum, which appears distinct from the rest of the brain and shows a different structure as well, can be used. The cerebellum is highlighted in **Figure 16** with a red circle. It is located at the back of the head.

The rotations and translations that are applied to the original PET images for realignment are shown in **Figure 17**. One subject was chosen arbitrarily for visualisation of this particular registration. Translations along the three spatial coordinate axes x, y and z are drawn in blue, green and red respectively. The same colours are used as well for the rotations about x (pitch), y (roll) and z (yaw). It can be seen that the first few images of the time series experience the largest changes with respect to the parameters of the transformation. Additionally, estimated translations and rotations increase towards the end of the time series.

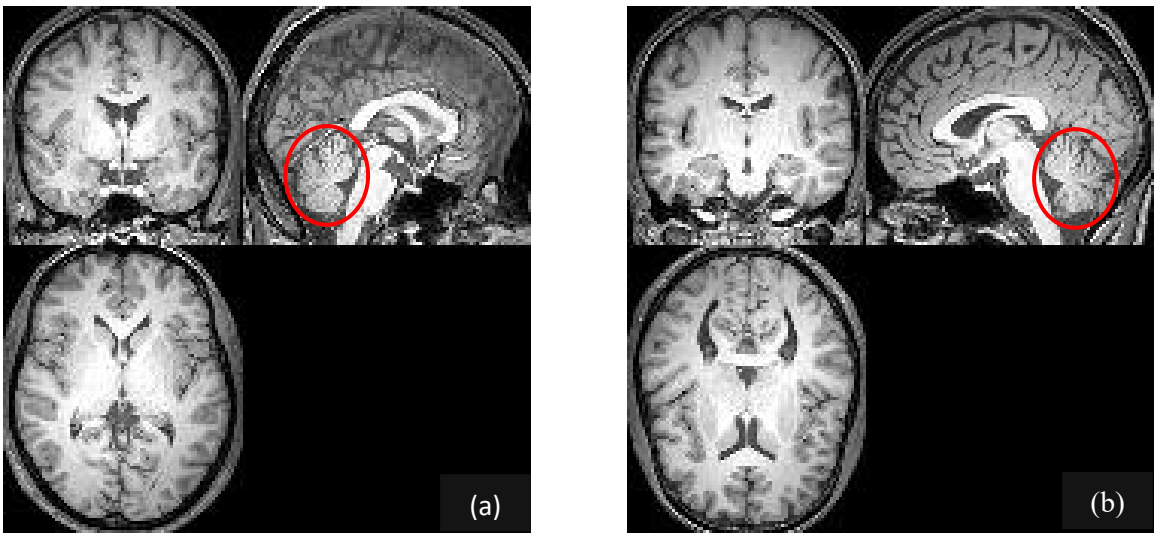

Figure 16: *coronal view (top left), sagittal view (top right) and transverse view (bottom left) of normalised T1 images for comparing different anterior-posterior orientations; The cerebellum is indicated with a red circle.* ***(a)*** *sagittal view: anterior = left;* ***(b)*** *sagittal view: anterior = right*

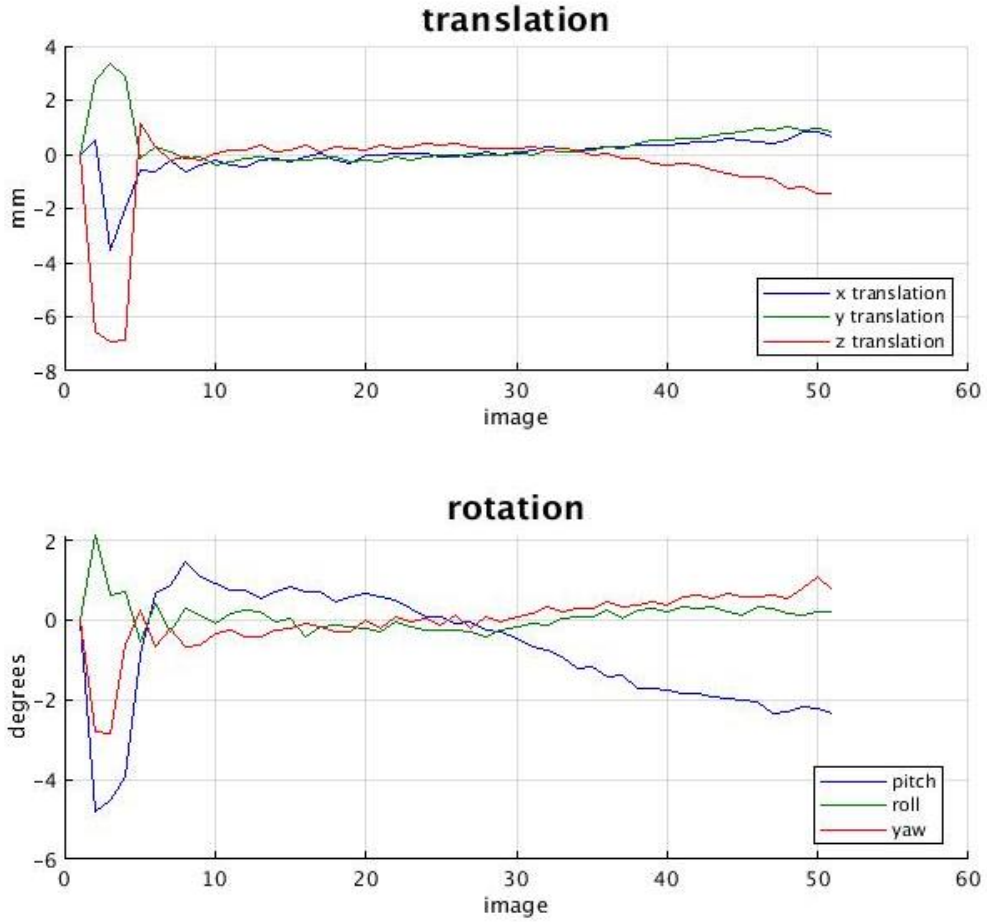

Figure 17: *translations and rotations for each image of the time series during realignment displayed for one subject*

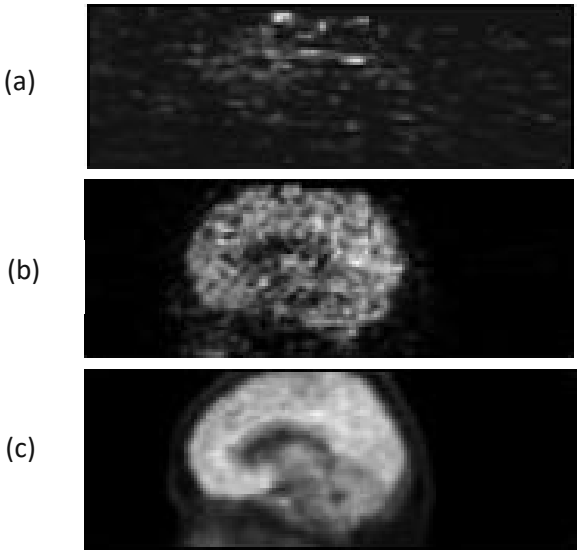

Figure 18: *comparison of first acquired volume* ***(a)****, volume fifteen* ***(b)*** *of time series and mean PET image* ***(c)***

When referring to **Figure 18** the need of using the mean image for registration of PET data becomes apparent. It shows a comparison of the first and 15th acquired volume in the time series as well as the mean image. While the first (**Figure 18 (a)**) shows no discernible features, volume number 15 shows at least the resemblance of the details available in the mean image. **Figure 18 (c)** shows by far the best signal to noise ratio.

The joint histograms before and after co-registration are shown in **Figure 19.** The joint histograms were calculated for the weighted mean image of the realigned PET data and the T1 weighted MRI scan. As expected, changes in the histogram are apparent in **Figure 19**.

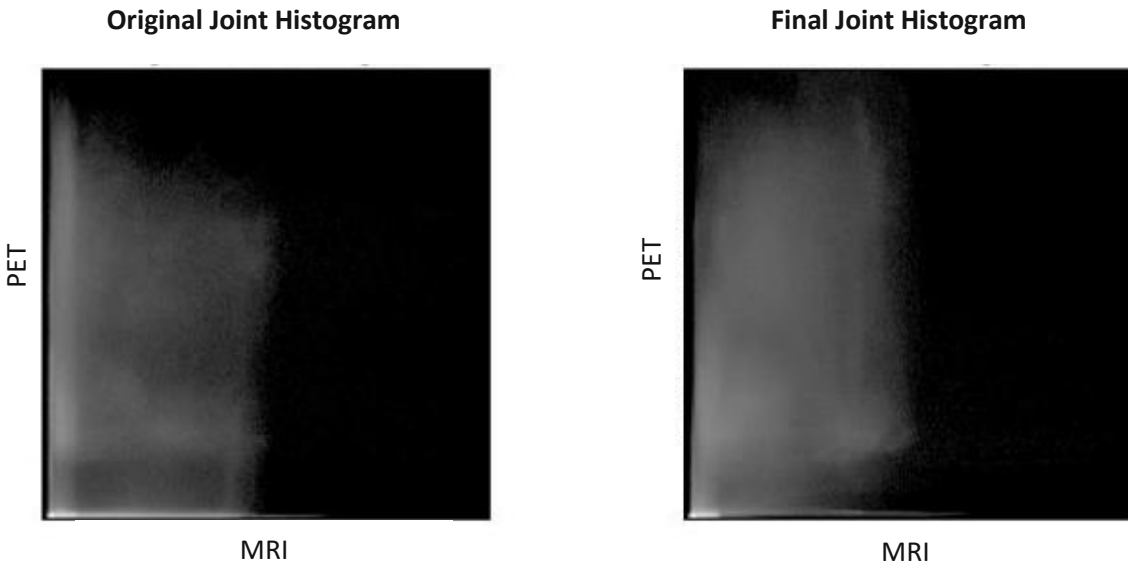

Figure 19: *joint histograms before (left) and after (right) registration of mean PET image to T1 image*

Figure 20 is a visualisation of the output resulting from normalisation for one subject. Mean PET image, T1 weighted MRI image and the tissue probability map are displayed. Using SPM12 for visualisation and moving the crosshair along distinct borders, showed that the normalisation was successful, because the crosshair position correspond between images. Investigated structures were the brain-air border, ventricle and longitudinal fissure. Since perfect correspondence between structures could not be expected, a certain discrepancy had to be accepted (especially for the lower-resolution PET image). For visualisation the mean PET image was used, as can be seen by the blurred nature of **Figure 20 (a)**. The reasoning for choosing the mean imager over a volume of the time series is also explained above in the discussion of **Figure 18**. As expected, it can be observed that the form of the three brain images is roughly the same after normalisation.

For patients where the T1 scan had been incorrectly aligned concerning the anterior-posterior orientation, co-registration and normalisation produced images devoid of any resemblance to a human brain. These scans were reprocessed with correct orientation.

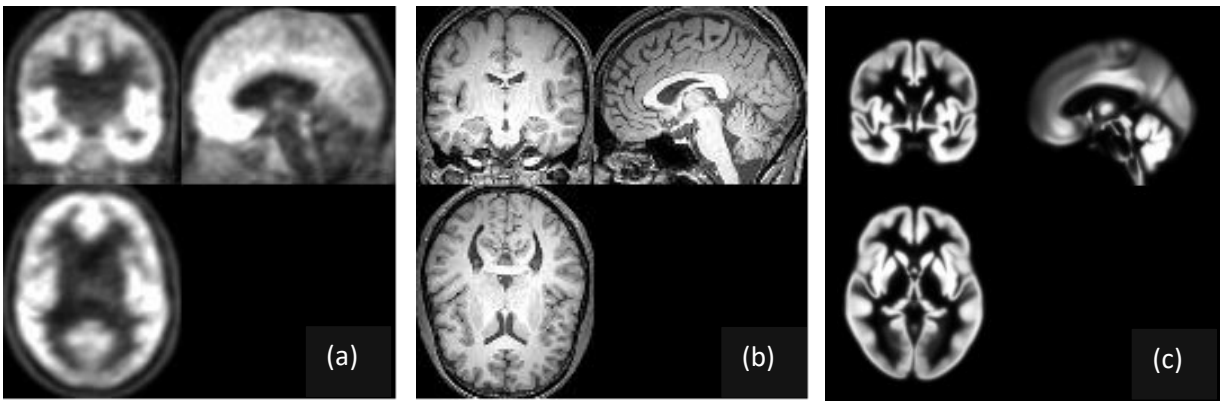

Figure 20: (a) *Mean of normalised PET,* ***(b)*** *normalised T1 scan and* ***(c)*** *template*

4.2 Modelling BP_{ND}

Before the model was calculated, PMOD displays the measured TACs as well as the modelled TAC. For one subject, these results are shown in **Figure 21**. Time activity curves for the receptor rich region (blue and grey) and the receptor-less region (orange) are easily discerned by the lower activity in CWM compared to the insula. The target region's measured and modelled data show similar behaviour. After an initial peak at the start of the measurement, activity starts to decrease again. In the reference region, activity approaches zero within 20 minutes after a smaller peak in the beginning, whereas in the insula an approximately linear decrease can be seen. The receptor-rich region still exhibits significantly increased activity after 90 minutes at the end of the measurement.

Due to the model's maximum acceptable error of 10%, activity was set to zero for the first few data points which had to be excluded to meet this constraint. For the subject data shown in **Figure 21**, the first value was set to zero (grey data point).

A merged image of modelled BP_{ND} and an anatomical template is shown in **Figure 22**. Regions of higher binding are shown in red. It can be seen that among other regions, left and right insula exhibit higher uptake whereas the cerebellum is in comparison devoid of activity.

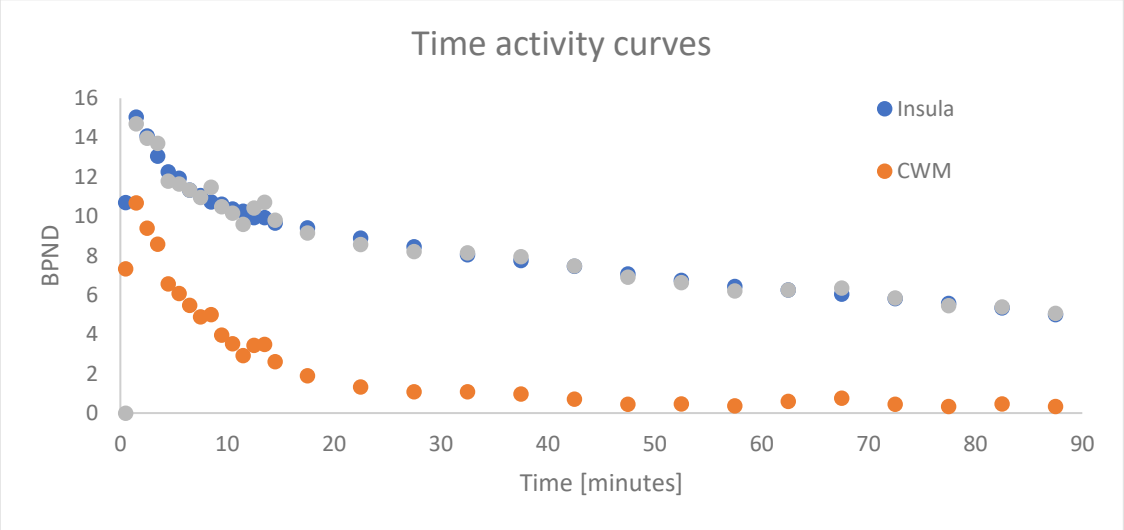

Figure 21: *measured and modelled time activity curves for a total acquisition time of 90 minutes; blue: measured TAC in insula; grey: modelled TAC in insula; orange: measured TAC in cerebral white matter*

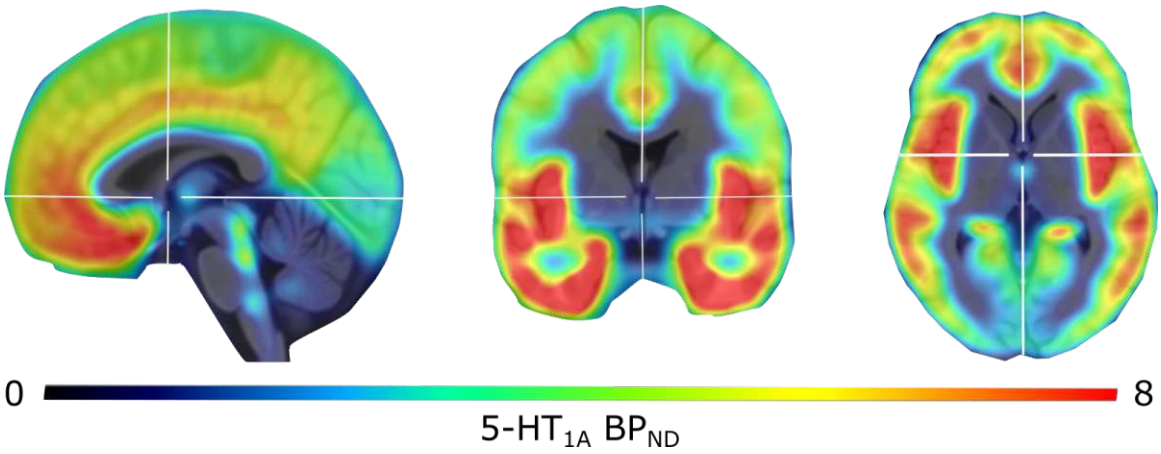

Figure 22: *mean 5-HT$_{1A}$ BP$_{ND}$ of healthy control superimposed on T1 weighted MRI image in MNI space; crosshair at x = 1, y = 0, z = 0 in MNI space*

4.3 Statistical Analysis

The normal Q-Q plots for visual validation of normal distribution are shown in **Figure 23**. Normal distribution is shown by the solid black line. The observed values for all ROIs and patient as well as healthy control group adhere reasonably well to normal distribution. Therefore, based on the Q-Q plots, normal distribution was not rejected for any population. In addition to this visual method, the results of the Shapiro-Wilk test show the same result. **Table 6** summarises the outcomes of the normality test for both groups and all regions. Even though, the data of the healthy controls in the amygdala show by far the lowest p-value (0.07), it still does not fall below the critical value of 0.05. Consequently, the Null hypothesis of normal distribution was not rejected for any region, thus meeting the criteria of normality for the repeated measures ANOVA.

Mauchly's sphericity test was used to evaluate the other prerequisite of the repeated measures ANOVA. The resulting p-value of 0.002 falls below the critical value (0.05). Consequently, the assumption of sphericity was rejected. Due to the lack of sphericity, the Greenhouse-Geisser correction was applied in the calculation of the repeated measures ANOVA.

Table 6: *p-values for Shapiro-Wilk Test for evaluating assumption of normally distributed harmonised* BP_{ND} *in the five regions of interest in patient and healthy control group*

	ACC	**INS**	**AMY**	**HIP**	**OFC**
HC	0.44	0.21	0.07	0.35	0.53
PAT	0.35	0.62	0.35	0.27	1

Before performing the repeated measures ANOVA, the data was visualised. **Figure 24** shows the bar chart of mean BP_{ND} for healthy control and patient population, grouped by region. Purely based on this figure it might be assumed that the means in the TRD group are lower for all regions than in the control group. However, the error bars ($mean \pm sd$) give a large overlap making it unclear to judge the hypothesis solely based on visual inspection. Moreover, the effect of region cannot be clearly judged as well.

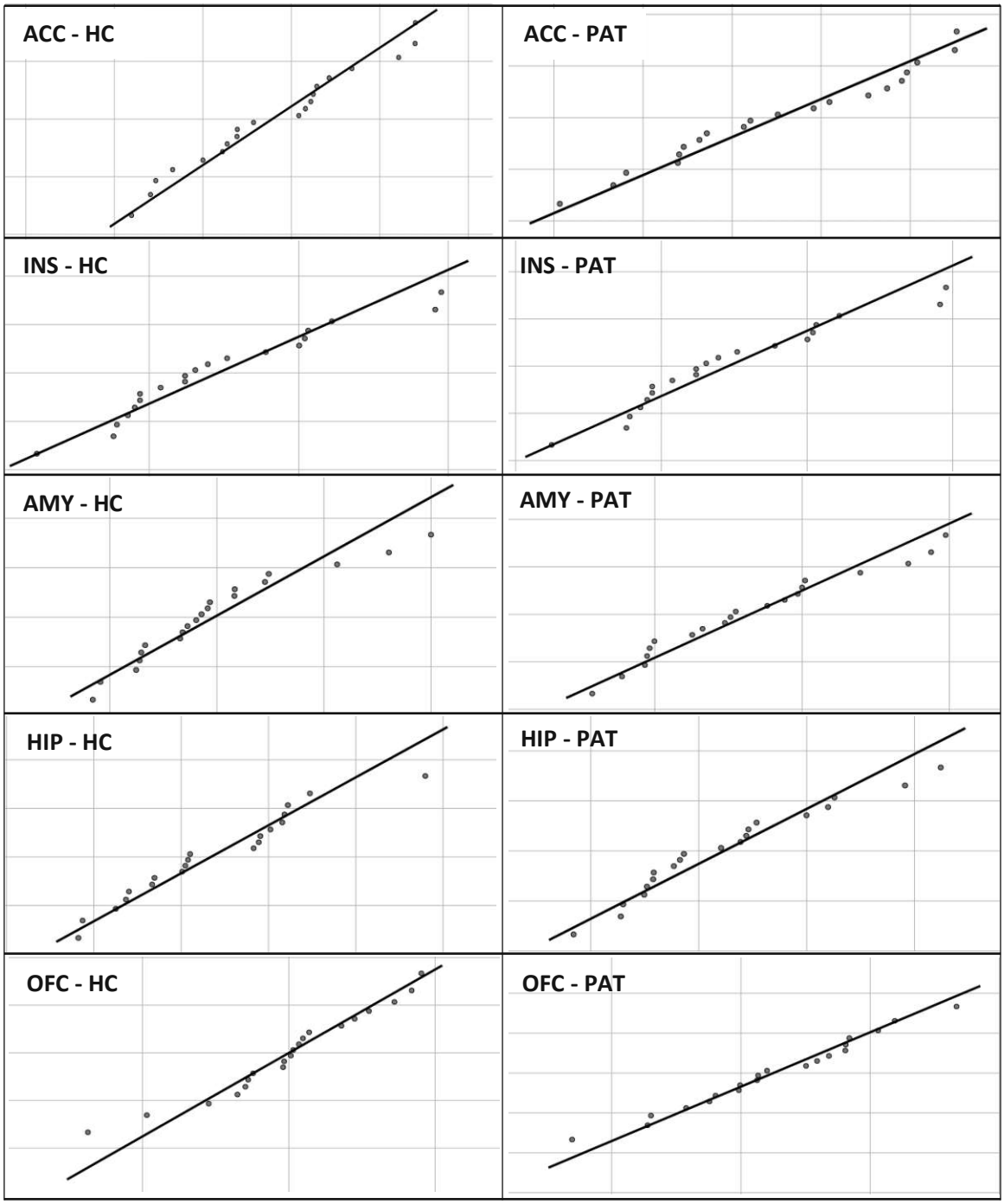

Figure 23: *normal Q-Q plots of the five ROIs for healthy control (HC) and patient group (PAT) used to evaluate normal distribution of residuals; solid line: expected normal distribution; dots: observed value; insula (INS), amygdala (AMY), orbitofrontal cortex (OFC), hippocampus (HIP) and anterior cingulate cortex (ACC)*

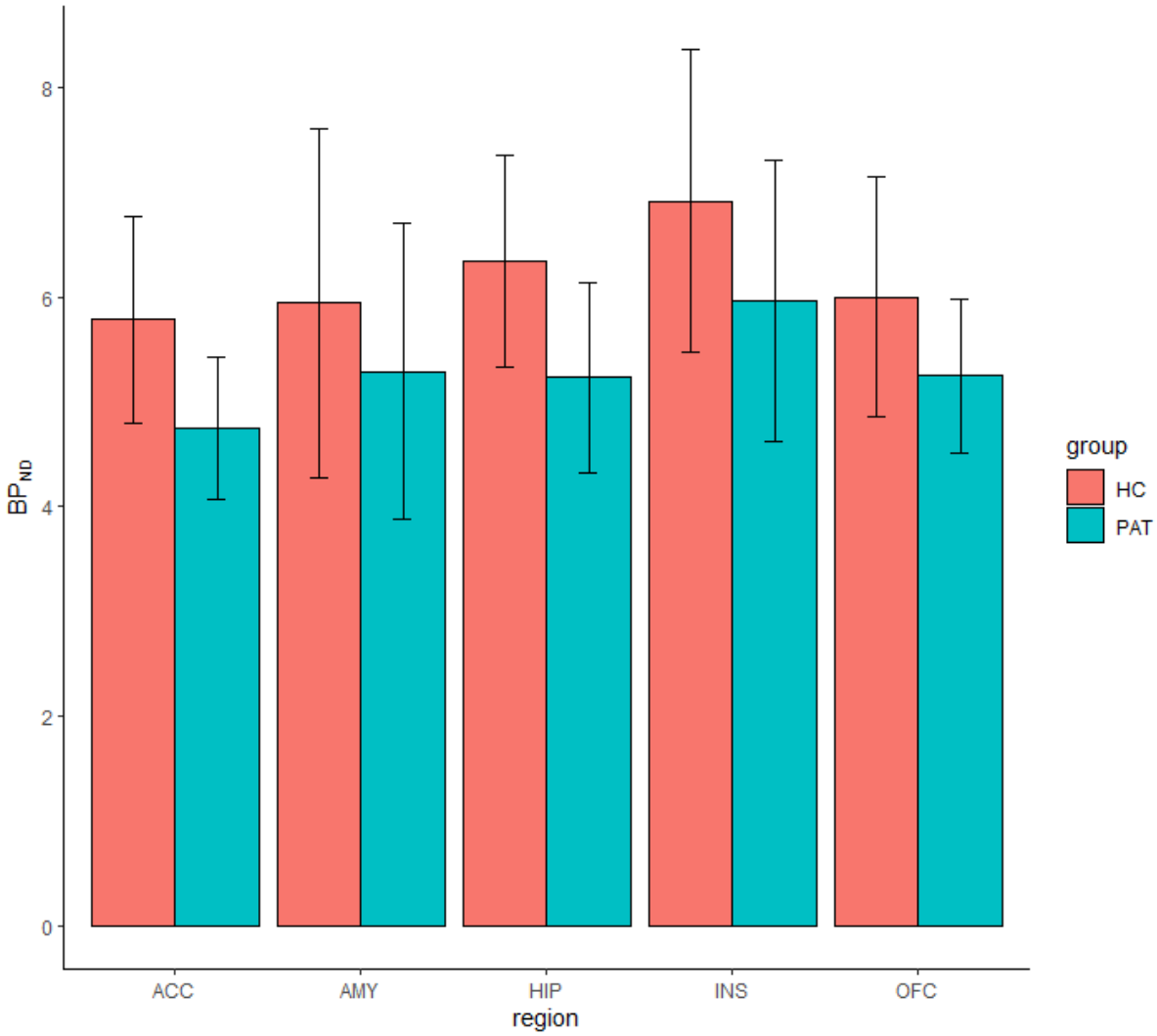

Figure 24: *mean ± sd of harmonised BP_{ND} for healthy control (HC) and patient (PAT) group; insula (INS), amygdala (AMY), orbitofrontal cortex (OFC), hippocampus (HIP) and anterior cingulate cortex (ACC)*

Following the evaluation of prerequisites, the repeated measures ANOVA was performed. The results are summarised in **Table 7**. The reported values were obtained using the Greenhouse-Geisser correction. The main effects of region and group show a p-value below 0.01. Since the p-values fall below the critical value of 0.05, it is concluded that region and group have a significant effect on BP_{ND}. However, the interaction effect with a p-value of 0.81 is not significant.

Table 7: summary of repeated measures ANOVA, including main effects of region and group as well as their interaction term (region*group); degrees of freedom (df), sum of squared error (SSE), mean squared error (MSE)

	df	**SSE**	**MSE**	**F**	**p**
region	2.95	29.71	10.09	6.47	< 0.01*
group	41	40.39	40.39	17.39	< 0.01*
region*group	2.95	1.43	0.49	0.31	0.81
residuals	111.91	174.47	1.39		

*p < 0.05

Since the repeated measures ANOVA showed a significant main effect of group, but not for the interaction of group and region, mean BP_{ND} was compared between the patient and healthy control group. Firstly, the assumptions for the two-sample t-test were examined. Levene's test of homogeneity of variance resulted in a p-value of 0.27. Consequently, the Null hypothesis of homoscedasticity was not rejected. In order to investigate normal distribution of the two populations, the Shapiro-Wilk test was performed. As seen in **Table 8**, patient and healthy control group show significant p-values at a significance level of 0.05. Therefore, the normality is rejected for both groups. As a result, the non-parametric, Independent-Samples Mann-Whitney U test was used instead of the two-sample t-test.

Table 8: *results of Shapiro-Wilk test for harmonised BP_{ND} in patient and healthy control group*

	PAT	**HC**
p-value	0.01*	0.03*

*p < 0.05

The Independent-Samples Mann-Whitney U Test resulted in a significant p-value ($p < 0.001$). With a p-value below the critical value of 0.05, the Null hypothesis that mean BP_{ND} is the same in healthy control and patient group was rejected. Mean BP_{ND} ± sd of the two populations is also shown in **Figure 25**. The patient group has a significantly lower BP_{ND} (5.3 ± 1.1) compared to the healthy control group (6.2 ± 1.3).

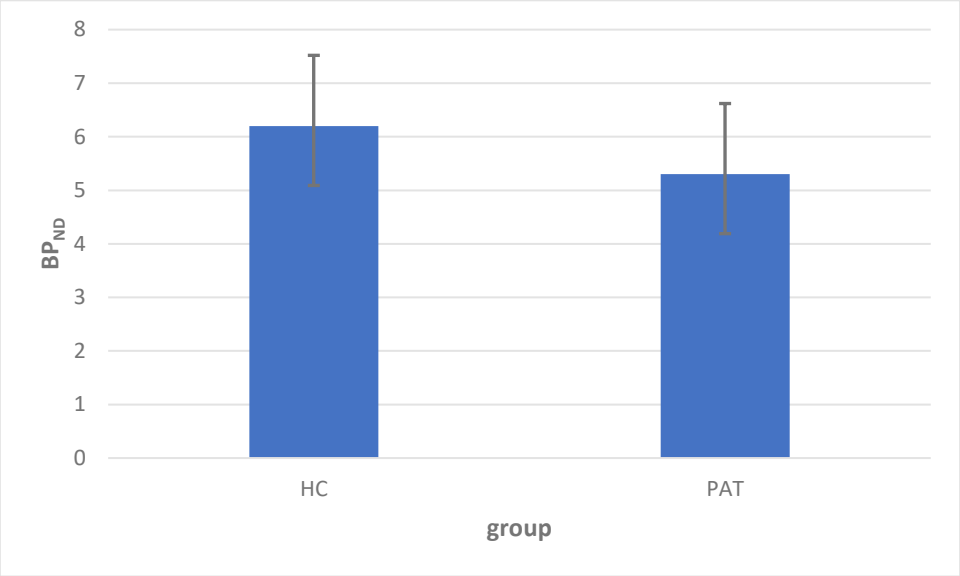

Figure 25: *mean BP_{ND} ± sd of healthy control and patient group averaged across the five brain regions*

5 Discussion

5.1 Preprocessing

Pre-processing produced acceptable outcomes at default parameters for all but one subject. This subject was reprocessed with adjustments made to the sampling distance for normalisation. It is not surprising that for realignment, the largest amount of translations and rotations were estimated for approximately the first five acquired volumes. These volumes are acquired closest to application of the tracer, thus making it possible that less tracer has had chance to accumulate in the brain than for later volumes. Moreover, the acquisition time in the beginning is the shortest. All in all this suggests low signal to noise ratio and as a result might lead to overestimating of the transformation parameters. Besides at the beginning of the scan, higher estimates of motion parameters also appear towards the end. This is another unsurprising behaviour, due to the PET scan's duration of 90 minutes.

The minor changes between the joint histograms (**Figure 19**) before and after normalisation are to be expected. The change depends on how well the images (in this case PET and T1) overlap before co-registration. Ideally, in the case of hybrid imaging with a hybrid PET-MRI system, patient placement would correspond even better between modalities resulting in minimal changes between joint histograms. Similar to the pre-processing, the modelling resulted in satisfactory outcomes for all subjects.

5.2 The 5-HT_{1A} Receptor

The 5-HT_{1A} receptor is located primarily presynaptically in the raphe nuclei, but postsynaptically everywhere else in the brain, where it has local inhibitory effects on neuronal activity (Saulin et al., 2012). Research on the implications of this receptor in psychiatric disorders has been mainly focused on its postsynaptic occurrences. Among other regions, highest abundance of the postsynaptic 5-HT_{1A} receptor has been shown in the ROIs that were investigated in this master thesis (HIP, AMY, OFC, INS, and ACC). Additionally, the cingulate cortex in general and the midbrain raphe regions display high receptor density as well (Hornung, 2010). Contrary, small numbers of 5-HT_{1A} receptor have been reported for the cerebellum and basal ganglia (Saulin et al., 2012).

While the reference tissue model requires a reference region devoid of specific binding, the cerebellum has been shown to express the 5-HT_{1A} receptor during childhood and sometimes also in adolescents (Hirvonen et al., 2007). Indeed, modelling of BP_{ND} yielded comparatively low but non-zero values in cerebellar white matter. Still, the use of CWM

has been demonstrated as a suitable choice for modelling 5-HT_{1A} binding potential (Parsey et al., 2000).

The repeated measures ANOVA with the Greenhouse-Geisser correction to account for lack of sphericity showed significant effects of group and region but not for their interaction. This indicates no regional variability in the difference of 5-HT_{1A} binding between groups, thus no post-hoc tests were performed for the effect of region. Even though, the TRD and healthy control groups were not compared separately for all regions, due to the lack of an interaction effect, a significant effect of group could be shown, when pooling the ROIs. Ultimately, it was shown that the mean BP_{ND} was lower in subjects with treatment resistant depression (5.3 ± 1.1, mean ± sd across regoins) compared to the healthy control group (6.2 ± 1.3).

Several other studies have shown similar alterations in 5-HT_{1A} receptors in major depression disorder. Generally, a decrease in nondisplaceable binding potential has been reported across most brain regions (Hirvonen et al., 2008; Saulin et al., 2012). However, some studies also show an increase in BP_F in medication naïve MDD subjects (Miller et al., 2009; Parsey et al., 2010). Methodological differences need to be considered when comparing these measures of binding potential, making direct comparisons difficult. While for BP_{ND} the specific uptake is compared to nondisplaceable uptake, BP_F compares it to the free plasma concentration (Innis et al., 2007). Moreover, heterogeneous image acquisition, processing, modelling and previous exposure to medication have been put forward as an explanation for the discrepancies of the reported differences between HC and MDD groups (Parsey et al., 2006). Finally, the effect of the reference region must not be neglected. If alterations in the reference region (CWM in this thesis) between control and patient group were present, BP_{ND} would be biased. In this case, it would not be possible to differentiate between changes in BP_{ND} due to differences in reference region or specific receptor binding in the target region. This potential issue could be avoided by future work which includes arterial blood sampling and quantification independent of a reference region. For MDD patients, the majority of studies show however similar results between BP_{ND} and BP_P, but as mentioned above not for BP_F (Hirvonen et al., 2008; Saulin et al., 2012).

A clinically relevant aspect would be a subsequent evaluation of patients with MDD and those with TRD compared to healthy controls. This could reveal if commonly observed decreases in 5-HT_{1A} binding in MDD are even more pronounced in TRD or if these reductions reach a plateau. The latter would be in line with reduced 5-HT_{1A} binding after long-term treatment with selective serotonin reuptake inhibitors (SSRI) in patients with anxiety disorders (Spindelegger et al., 2008). SSRIs represent the first-line pharmacological treatment option for these two patient groups that show high comorbidity among each other. Thus, an additional decrease in 5-HT_{1A} binding after treatment might indicate a lack of required adaptive effects in MDD and TRD. Alternatively, interactions at the systems level need to be considered. Among others this include changes in both pre- and postsynaptic 5-HT1A binding as well as other receptor subtypes of the serotonin system and potentially further neurotransmitters.

5.3 Limitations

A number of limitations have been found for this master thesis. Firstly, the pre-processing was performed by two different people for the HC and TRD groups. This may introduce a bias, although use of the same algorithms should mitigate this issue. Secondly, the limited experience of the author may lead to too high acceptance in results that had to be visually confirmed, such as the output of the normalisation and modelling. However, this limitation was mitigated by consulting experienced colleagues. Finally, the design of this study might measure the combined effect of MDD and TRD. As mentioned above, a more relevant study design might be comparing MDD patients to patients with TRD.

5.4 Conclusion and Outlook

While alterations of the 5-HT_{1A} receptor in MDD are well documented, studies on the implications for TRD are relatively sparse. The findings presented in this master thesis further support the notion that TRD might have an effect on the 5-HT_{1A} receptor similar to MDD. Additional research in this area might lead to a better understanding of the condition. If other analyses show comparable differences in the 5-HT_{1A} receptor between treatment resistant depression patients and healthy controls, prospective studies would be a valuable next step. In the future, the possibility of screening for TRD in MDD patients could be a promising addition to existing procedures.

6 Acronyms

5-HT$_{1A}$	5-hydroxytryptamine-1A
ACC	anterior cingulate cortex
ACD	annihilation incident detection
AMY	amygdala
ANOVA	analysis of variance
BP$_{ND}$	nondisplaceable binding potential
CSF	cerebrospinal fluid
CWM	cerebellar white matter
df	degrees of freedom
DSM	Diagnostic and Statistical Manual of Mental Disorders
fMRI	functional magnetic resonance imaging
FOV	field of view
HC	healthy control
HIP	hippocampus
ICD	International Classification of Diseases
ICRP	International Commission on Radiological Protection
INS	insula
MDD	major depressive disorder
MI	mutual information
MIRD	Medical Internal Radiation Dosimetry
MRI	magnetic resonance imaging
MRTM	multilinear reference tissue model
MSE	mean squared error
NIL	Neuroimaging Labs
NMR	nuclear magnetic resonance
OFC	orbitofrontal cortex

PD	proton density
PET	positron emission tomography
RF	radiofrequency
ROI	region of interest
r_S	source region
r_T	target region
sd	standard deviation
SE	spin echo
SPECT	single photon emission tomography
SPM	statistical parametric mapping
SSE	sum of squared error
SSRI	selective serotonin reuptake inhibitor
TAC	time activity curve
TE	time of echo
TR	time of repetition
TRD	treatment resistant depression
V	distribution volume
WHO	World Health Organisation

7 Bibliography

Albert, P. R., & Lemonde, S. (2004). 5-HT1A receptors, gene repression, and depression: guilt by association. *The Neuroscientist*, *10*(6), 575–593. https://doi.org/10.1177/1073858404267382

American Psychiatric Association. (2022). *Diagnostic and Statistical Manual of Mental Disorders* (5th ed.). American Psychiatric Association.

Ashburner, J., Barnes, G., Chen, C.-C., Daunizeau, J., Flandin, G., Friston, K., Gitelman, D., Glauche, V., Henson, R., Hutton, C., Jafarian, A., Kiebel, S., Kilner, J., Litvak, V., Mattout, J., Moran, R., Penny, W., Phillips, C., Razi, A., & Zeidman, P. (2021). *SPM12 Manual*.

Ashburner, J., & Friston, K. J. (2005). Unified segmentation. *NeuroImage*, *26*(3), 839–851. https://doi.org/10.1016/J.NEUROIMAGE.2005.02.018

Baldinger, P., Höflich, A. S., Mitterhauser, M., Hahn, A., Rami-Mark, C., Spies, M., Wadsak, W., Lanzenberger, R., & Kasper, S. (2014). Effects of Silexan on the serotonin-1A receptor and microstructure of the human brain: a randomized, placebo-controlled, double-blind, cross-over study with molecular and structural neuroimaging. *The International Journal of Neuropsychopharmacology*, *18*(4), 1–9. https://doi.org/10.1093/IJNP/PYU063

Bartova, L., Dold, M., Kautzky, A., Fabbri, C., Spies, M., Serretti, A., Souery, D., Mendlewicz, J., Zohar, J., Montgomery, S., Schosser, A., & Kasper, S. (2019). Results of the European Group for the Study of Resistant Depression (GSRD) - basis for further research and clinical practice. *The World Journal of Biological Psychiatry : The Official Journal of the World Federation of Societies of Biological Psychiatry*, *20*(6), 427–448. https://doi.org/10.1080/15622975.2019.1635270

Bushberg, J. T., Seibert, A. J., Leiholdt, E. M., & Boone, J. M. (2012). The Essential Physics of Medical Imaging. In J. T. Bushberg, A. J. Seibert, E. M. Leiholdt, & J. M. Boone (Eds.), *The Essential Physics of Medical Imaging* (3rd ed.). Lippincott Williams & Wilkins.

Cherry, S., Sorenson, J., & Phelps, M. (2012). *Physics in Nuclear Medicine* (3rd ed.). Saunders.

Collignon, A., Maes, F., Delaere, D., Vandermeulen, D., Suetens, P., & Marchal, G. (1995). Automated multi-modality image registration based on information theory. In Y. Bizais, C. Barillot, & R. di Paola (Eds.), *Information Processing in Medical Imaging* (pp. 263–274). Kluwer Academic Publishers.

Conejero, I., Olié, E., Calati, R., Ducasse, D., & Courtet, P. (2018). Psychological Pain, Depression, and Suicide: Recent Evidences and Future Directions. *Current Psychiatry Reports*, *20*(5). https://doi.org/10.1007/S11920-018-0893-Z

Cristy, M., & Eckerman, K. F. (1987). Specific Absorbed Fractions of Energy at Various Ages from Internal Photon Sources. In *ORNL Report ORNL/TM-12907*. Oak Ridge National Labs.

Dar, K. A., Iqbal, N., & Mushtaq, A. (2017). Intolerance of uncertainty, depression, and anxiety: Examining the indirect and moderating effects of worry. *Asian Journal of Psychiatry*, *29*, 129–133. https://doi.org/10.1016/J.AJP.2017.04.017

Dold, M., & Kasper, S. (2017). Evidence-based pharmacotherapy of treatment-resistant unipolar depression. *International Journal of Psychiatry in Clinical Practice*, *21*(1), 13–23. https://doi.org/10.1080/13651501.2016.1248852

Farde, L., Ito, H., Swahn, C., Pike, V., & CJ, H. (1998). Quantitative analyses of carbonyl-carbon-11-WAY-100635 binding to central 5-hydroxytryptamine-1A receptors in man. *Journal of Nuclear Medicine* , *39*, 1965–1971.

Fornaro, M., & Giosuè, P. (2010). Current Nosology of Treatment Resistant Depression: A Controversy Resistant to Revision. *Clinical Practice & Epidemiology in Mental Health*, *6*, 20–24.

Forster, E. A., Cliffe, I. A., Bill, D. J., Dover, G. M., Jones, D., Reilly, Y., & Fletcher, A. (1995). A pharmacological profile of the selective silent 5-HT1A receptor antagonist, WAY-100635. *European Journal of Pharmacology*, *281*(1), 81–88. https://doi.org/10.1016/0014-2999(95)00234-C

Fortin, J. P., Cullen, N., Sheline, Y. I., Taylor, W. D., Aselcioglu, I., Cook, P. A., Adams, P., Cooper, C., Fava, M., McGrath, P. J., McInnis, M., Phillips, M. L., Trivedi, M. H., Weissman, M. M., & Shinohara, R. T. (2018). Harmonization of cortical thickness measurements across scanners and sites. *NeuroImage*, *167*, 104–120. https://doi.org/10.1016/J.NEUROIMAGE.2017.11.024

Fortin, J. P., Parker, D., Tunç, B., Watanabe, T., Elliott, M. A., Ruparel, K., Roalf, D. R., Satterthwaite, T. D., Gur, R. C., Gur, R. E., Schultz, R. T., Verma, R., & Shinohara, R. T. (2017). Harmonization of multi-site diffusion tensor imaging data. *NeuroImage*, *161*, 149–170. https://doi.org/10.1016/J.NEUROIMAGE.2017.08.047

Frackowiak, R. S. J., Friston, K. J., Frith, C. D., Dolan, R. J., Price, C. J., Zeki, S., Ashburner, J. T., & Penny, W. D. (Eds.). (2004). Chapter 31 - Experimental Design and Statistical Parametric Mapping. In *Human Brain Function (Second Edition)* (pp. 599–632). Academic Press. https://doi.org/https://doi.org/10.1016/B978-012264841-0/50033-0

Friston, K. J. (2004). Rigid Body Registration. In R. S. J. Frackowiak, C. D. Frith, C. J. Price, J. T. Ashburner, K. J. Friston, R. J. Dolan, S. Zeki, & W. D. Penny (Eds.), *Human Brain Function* (2nd ed., pp. 635–653). Academic Press.

Friston, K. J., Ashburner, J., Frith, C. D., Poline, J. -B, Heather, J. D., & Frackowiak, R. S. J. (1995). Spatial registration and normalization of images. *Human Brain Mapping*, *3*(3), 165–189. https://doi.org/10.1002/HBM.460030303

Global Burden of Disease Collaborative Network. (2020). *Global Burden of Disease Study 2019 (GBD 2019) Results*. https://vizhub.healthdata.org/gbd-results/

Hill, D. L. G., Batchelor, P. G., Holden, M., & Hawkes, D. J. (2001). Medical image registration. *Physics in Medicine and Biology*, *46*.

Hirvonen, J., Kajander, J., Allonen, T., Oikonen, V., Någren, K., & Hietala, J. (2007). Measurement of serotonin 5-HT1A receptor binding using positron emission tomography and [carbonyl-11C]WAY-100635 - Considerations on the validity of cerebellum as a reference region. *Journal of Cerebral Blood Flow and Metabolism*, *27*(1), 185–195. https://doi.org/10.1038/sj.jcbfm.9600326

Hirvonen, J., Karlsson, H., Kajander, J., Lepola, A., Markkula, J., Rasi-Hakala, H., Någren, K., Salminen, J. K., & Hietala, J. (2008). Decreased brain serotonin 5-HT1A receptor availability in medication-naive patients with major depressive disorder: an in-vivo imaging study using PET and [carbonyl-11C]WAY-100635. *International Journal of Neuropsychopharmacology*, *11*(4), 465–476. https://doi.org/10.1017/S1461145707008140

Hornung, J. P. (2010). The Neuronatomy of the Serotonergic System. In p, C. Müller & L. B. Jacobs (Eds.), *Handbook of Behavioral Neuroscience* (Vol. 21, Issue C, pp. 51–64). Academic Press. https://doi.org/10.1016/S1569-7339(10)70071-0

Ichise, M., Ballinger, J. R., Golan, H., Vines, D., Luong, A., Tsai, S., & Kung, H. F. (1996). Noninvasive Quantification of Dopamine D2 Receptors with Iodine-123-IBF SPECT. *Journal of Nuclear Medicine*, *37*(3).

Ichise, M., Liow, J. S., Lu, J. Q., Takano, A., Model, K., Toyama, H., Suhara, T., Suzuki, K., Innis, R. B., & Carson, R. E. (2003). Linearized reference tissue parametric imaging methods: application to [11C]DASB positron emission tomography studies of the serotonin transporter in human brain. *Journal of Cerebral Blood Flow and Metabolism*, *23*(9), 1096–1112. https://doi.org/10.1097/01.WCB.0000085441.37552.CA

Innis, R. B., Cunningham, V. J., Delforge, J., Fujita, M., Gjedde, A., Gunn, R. N., Holden, J., Houle, S., Huang, S. C., Ichise, M., Iida, H., Ito, H., Kimura, Y., Koeppe, R. A., Knudsen, G. M., Knuuti, J., Lammertsma, A. A., Laruelle, M., Logan, J., … Carson, R. E. (2007). Consensus nomenclature for in vivo imaging of reversibly binding radioligands. *Journal of Cerebral Blood Flow and Metabolism*, *27*(9), 1533–1539. https://doi.org/10.1038/sj.jcbfm.9600493

Johnson, W. E., Li, C., & Rabinovic, A. (2007). Adjusting batch effects in microarray expression data using empirical Bayes methods. *Biostatistics*, *8*(1), 118–127. https://doi.org/10.1093/BIOSTATISTICS/KXJ037

Kaufman, J., DeLorenzo, C., Choudhury, S., & Parsey, R. v. (2016). The 5-HT1A receptor in Major Depressive Disorder. *European Neuropsychopharmacology : The Journal of the European College of Neuropsychopharmacology*, *26*(3), 397. https://doi.org/10.1016/J.EURONEURO.2015.12.039

Klimont, J. (2020). *Österreichische Gesundheitsbefragung 2019*.

Krasikova, R. N., Andersson, J., Truong, P., Nag, S., Shchukin, E. v., & Halldin, C. (2009). A fully automated one-pot synthesis of [carbonyl-11C]WAY-100635 for clinical PET applications. *Applied Radiation and Isotopes*, *67*(1), 73–78. https://doi.org/10.1016/J.APRADISO.2008.07.008

Kuperman, V. (2000). Magnetic Resonance Imaging: Physical Principles and Applications. In *Magnetic Resonance Imaging: Physical Principles and Applications*. Academic Press.

Lanzenberger, R., Baldinger, P., Hahn, A., Ungersboeck, J., Mitterhauser, M., Winkler, D., Micskei, Z., Stein, P., Karanikas, G., Wadsak, W., Kasper, S., & Frey, R. (2013). Global decrease of serotonin-1A receptor binding after electroconvulsive therapy in major depression measured by PET. *Molecular Psychiatry*, *18*(1), 93. https://doi.org/10.1038/MP.2012.93

Lanzenberger, R., Mitterhauser, M., Spindelegger, C., Wadsak, W., Klein, N., Mien, L. K., Holik, A., Attarbaschi, T., Mossaheb, N., Sacher, J., Geiss-Granadia, T., Kletter, K., Kasper, S., & Tauscher, J. (2007). Reduced serotonin-1A receptor binding in social anxiety disorder. *Biological Psychiatry*, *61*(9), 1081–1089. https://doi.org/10.1016/J.BIOPSYCH.2006.05.022

Leach, M. O. (2014). Magnetic Resonance Imaging. In D. R. Dance, S. Christofides, A. ,D, A. Maidment, I. D. McLean, & K. H. Ng (Eds.), *Diagnostic Radiology Physics: A Handbook for Teachers and Students*. International Atomic Energy Agency.

Lui, S., Zhou, X. J., Sweeney, J. A., & Gong, Q. (2016). Psychoradiology: The Frontier of Neuroimaging in Psychiatry. *Https://Doi.Org/10.1148/Radiol.2016152149*, *281*(2), 357–372. https://doi.org/10.1148/RADIOL.2016152149

Maes, F., Loeckx, D., Vandermeulen, D., & Suetens, P. (2015). Image registration using mutual information. In N. Paragios, J. Duncan, & N. Ayache (Eds.), *Handbook of Biomedical Imaging: Methodologies and Clinical Research* (pp. 295–308). Springer.

Maisey, M. N. (2005). Physics and Instrumentation in PET. In D. L. Bailey, D. W. Townsend, P. E. Valk, & M. N. Maisey (Eds.), *Positron Emission Tomography: Basic Sciences* (pp. 13–39). Springer . https://doi.org/10.1007/1-84628-007-9_2

McRobbie, D. W., Moore, E. A., Graves, M. J., & Prince, M. R. (2006). *MRI from Picture to Proton* (2nd ed.). Cambridge University Press. https://doi.org/DOI: 10.1017/CBO9780511545405

Meikle, S. R., & Badawi, R. D. (2005). Quantitative Techniques in PET. In D. L. Bailey, D. W. Townsend, P. E. Valk, & M. N. Maisey (Eds.), *Positron Emission Tomography* (pp. 93–126). Springer.

Miller, J. M., Brennan, K. G., Ogden, T. R., Oquendo, M. A., Sullivan, G. M., Mann, J. J., & Parsey, R. v. (2009). Elevated Serotonin 1A Binding in Remitted Major Depressive Disorder: Evidence for a Trait Biological Abnormality. *Neuropsychopharmacology : Official Publication of the American College of Neuropsychopharmacology*, *34*(10), 2275. https://doi.org/10.1038/NPP.2009.54

Mitelman, S. A. (2019). Transdiagnostic neuroimaging in psychiatry: A review. *Psychiatry Research*, *277*, 23–38. https://doi.org/10.1016/J.PSYCHRES.2019.01.026

Pandarakalam, J. P. (2018). Challenges of Treatment-resistant Depression. *Psychiatria Danubina*, *30*(3), 273–284. https://doi.org/10.24869/PSYD.2018.273

Parsey, R. v, Belanger, M.-J., Sullivan, G. M., Simpson, N. R., Stabin, M. G., van Heertum, R., & Mann, J. J. (2005). Biodistribution and Radiation Dosimetry of 11C-WAY100,635 in Humans. *Journal of Nuclear Medicine*, *46*(4), 614. http://jnm.snmjournals.org/content/46/4/614.abstract

Parsey, R. v., Ogden, R. T., Miller, J. M., Tin, A., Hesselgrave, N., Goldstein, E., Mikhno, A., Milak, M., Zanderigo, F., Sullivan, G. M., Oquendo, M. A., & Mann, J. J. (2010). Higher Serotonin 1A Binding

in a Second Major Depression Cohort: Modeling and Reference Region Considerations. *Biological Psychiatry*, *68*(2), 170. https://doi.org/10.1016/J.BIOPSYCH.2010.03.023

Parsey, R. v., Olvet, D. M., Oquendo, M. A., Huang, Y. Y., Ogden, R. T., & Mann, J. J. (2006). Higher 5-HT1A receptor binding potential during a major depressive episode predicts poor treatment response: Preliminary data from a naturalistic study. *Neuropsychopharmacology*, *31*(8), 1745–1749. https://doi.org/10.1038/SJ.NPP.1300992

Parsey, R. v., Slifstein, M., Hwang, D. R., Abi-Dargham, A., Simpson, N., Mawlawi, O., Guo, N. N., van Heertum, R., John Mann, J., & Laruelle, M. (2000). Validation and reproducibility of measurement of 5-HT1A receptor parameters with [carbonyl-11C]WAY-100635 in humans: comparison of arterial and reference tisssue input functions. *Journal of Cerebral Blood Flow and Metabolism*, *20*(7), 1111–1133. https://doi.org/10.1097/00004647-200007000-00011

Ribeiro, J. D., Huang, X., Fox, K. R., & Franklin, J. C. (2018). Depression and hopelessness as risk factors for suicide ideation, attempts and death: meta-analysis of longitudinal studies. *The British Journal of Psychiatry : The Journal of Mental Science*, *212*(5), 279–286. https://doi.org/10.1192/BJP.2018.27

Rinck, A. P. (2008). A short history of magnetic resonance imaging. *Spectroscopy Europe*, *20*(1).

Rischka, L., Gryglewski, G., Berroterán-Infante, N., Rausch, I., James, G. M., Klöbl, M., Sigurdardottir, H., Hartenbach, M., Hahn, A., Wadsak, W., Mitterhauser, M., Beyer, T., Kasper, S., Prayer, D., Hacker, M., & Lanzenberger, R. (2019). Attenuation Correction Approaches for Serotonin Transporter Quantification With PET/MRI. *Frontiers in Physiology*, *10*, 1422. https://doi.org/10.3389/FPHYS.2019.01422/BIBTEX

Saulin, A., Savli, M., & Lanzenberger, R. (2012). Serotonin and molecular neuroimaging in humans using PET. *Amino Acids*, *42*(6), 2039–2057. https://doi.org/10.1007/s00726-011-1078-9

Savli, M., Bauer, A., Häusler, D., Kroll, T., Hahn, A., Rattay, F., Mitterhauser, M., Wadsak, W., Kasper, S., & Lanzenberger, R. (2011). In vivo molecular imaging reveals distinct distributions of the serotonin transporter, the major inhibitory and excitatory serotonin receptors. *European Psychiatry*, *26*(S2), 953–953. https://doi.org/10.1016/S0924-9338(11)72658-X

Savli, M., Bauer, A., Mitterhauser, M., Ding, Y. S., Hahn, A., Kroll, T., Neumeister, A., Haeusler, D., Ungersboeck, J., Henry, S., Isfahani, S. A., Rattay, F., Wadsak, W., Kasper, S., & Lanzenberger, R. (2012). Normative database of the serotonergic system in healthy subjects using multi-tracer PET. *NeuroImage*, *63*(1), 447–459. https://doi.org/10.1016/J.NEUROIMAGE.2012.07.001

Shah, S. M. A., Mohammad, D., Qureshi, M. F. H., Abbas, M. Z., & Aleem, S. (2021). Prevalence, Psychological Responses and Associated Correlates of Depression, Anxiety and Stress in a Global Population, During the Coronavirus Disease (COVID-19) Pandemic. *Community Mental Health Journal*, *57*(1), 101–110. https://doi.org/10.1007/S10597-020-00728-Y

Shelton, R., Tollefson, G., & Tohen, M. (2007). A novel augmentation strategy for treatment resistant depression. *Eur Psychiatry*, 17 (Suppl 1)-98.

Shen, J. (2022). *Tools for NIfTI and ANALYZE image*. MATLAB Central File Exchange. https://de.mathworks.com/matlabcentral/fileexchange/8797-tools-for-nifti-and-analyze-image

Snyder, W., Warner, G., & Ford, M. (1978). Estimates of Specific Absorbed Fractions for Photon Sources Uniformly Distributed in Various Organs of a Heterogeneous Phantom. In *MIRD Pamphlet No. 5 (revised)*. Society of Nuclear Medicine.

Song, H. K. (2014). Physics of Magnetic Resonance. In D. R. Dance, S. Christofides, A. D. A. Maidment, I. D. McLean, & K. H. Ng (Eds.), *Diagnostic Radiology Physics: A Handbook for Teachers and Students*. International Atomic Energy Agency.

Spindelegger, C., Lanzenberger, R., Wadsak, W., Mien, L. K., Stein, P., Mitterhauser, M., Moser, U., Holik, A., Pezawas, L., Kletter, K., & Kasper, S. (2008). Influence of escitalopram treatment on 5-HT1A receptor binding in limbic regions in patients with anxiety disorders. *Molecular Psychiatry 2009 14:11*, *14*(11), 1040–1050. https://doi.org/10.1038/mp.2008.35

Sprawls, P. (2000). Magnetic Resonance Imaging: Principles, Methods and Techniques. In *Magnetic Resonance Imaging: Principles* (2nd ed., Issue 1). Medical Physics Publishing. https://doi.org/10.1007/BF03178286

Stabin, M. G., Watson, E. E., Cristy, M., Ryman, M., Eckerman, J. C., Davis, K. F., Marshall, D., & Gehlen, M. (1995). *Mathematical Models and Specific Absorbed Fractions of Photon Energy in the Nonpregnant Adult Female and at the End of Each Trimester of Pregnancy*.

Sutton, D., Collins, L. T., & Heron, J. le. (2014). Radiation Protection. In D. R. Dance, S. Christofides, A. D. A. Maidment, I. D. McLean, & K. H. Ng (Eds.), *Diagnostic Radiology Physics: a Handbook for Teachers and Students* (pp. 615–666). International Atomic energy Agency.

Towson, J. E. (2005). Radiation Dosimetry and Protection in PET. In D. L. Bailey, D. W. Townsend, P. E. Valk, & M. N. Maisey (Eds.), *Positron Emission Tomography* (pp. 251–266). Springer.

Turkheimer, F. E., Veronese, M., & Dunn, J. (2014). Experimental Design and Practical Data Analysis in Positron Emission Tomography. In *European Journal of Nuclear Medicine and Molecular Imaging 2014 42:6* (Issue 6).

UN General Assembly. (2007, January 24). *Convention on the Rights of Persons with Disabilities : resolution / adopted by the General Assembly*. https://www.ohchr.org/en/instruments-mechanisms/instruments/convention-rights-persons-disabilities

Vanes, L. D., & Dolan, R. J. (2021). Transdiagnostic neuroimaging markers of psychiatric risk: A narrative review. *NeuroImage: Clinical*, *30*, 102634. https://doi.org/10.1016/J.NICL.2021.102634

WHO. (2022a). *International Classification of Diseases Eleventh Revision (ICD-11)*. World Health Organization; 2022.

WHO. (2022b). *World health statistics 2022: monitoring health for the SDGs, sustainable development goals*. World Health Organization.

Yousaf, T., Dervenoulas, G., & Politis, M. (2018). Advances in MRI Methodology. *International Review of Neurobiology*, *141*, 31–76. https://doi.org/10.1016/BS.IRN.2018.08.008